

ABSTRACT

Title of Thesis: A METHOD FOR MEASUREMENT OF SPATIALLY RESOLVED RADIATION INTENSITY AND RADIATIVE FRACTION OF LAMINAR FLAMES OF GASEOUS AND SOLID FUELS

Catherine Marie Hamel, Master of Science,
2016

Thesis Directed By: Dr. Stanislav Stoliarov, Associate Professor,
Department of Fire Protection Engineering

This work introduces a new method for determination of the radiative fraction for axisymmetric laminar flames for both gaseous and solid fuels by using a DSL-R camera and a Schmidt-Boelter heat flux gauge. The high spatial resolution provided by the images of the camera allow for a multi-emitter treatment of the 2-6 cm flames. The flame's radius and intensity are extracted from the images and presented as two curves that are functions of the flame-axis position. Each point on the flame sheet is discretized at pixel-level resolution and treated as a differential emitting surface. Radiation transport equations are formulated and solved numerically to compute a function that relates the camera's readings to the total thermal radiation intensity detected by the

gauge. The calculation yields spatially resolved radiation intensity information. Integration of this intensity over the flame surface divided by the total heat release rate yields the global radiative fraction.

A METHOD FOR MEASUREMENT OF SPATIALLY RESOLVED
RADIATION INTENSITY AND RADIATIVE FRACTION OF LAMINAR
FLAMES OF GASEOUS AND SOLID FUELS

by

Catherine Marie Hamel

Thesis submitted to the Faculty of the Graduate School of the
University of Maryland, College Park, in partial fulfillment
of the requirements for the degree of
Master of Science
2016

Advisory Committee:

Professor Stanislav Stoliarov, Ph.D., Chair
Professor Marino diMarzo, Ph.D.
Professor Peter Sunderland, Ph.D.

© Copyright by
Catherine Marie Hamel
2016

Dedication

This work is dedicated to my parents, Catherine Hamel and Denis Hamel. Your continuous support and dedication to my education have gotten me to graduate school and have led me to being a lover of learning. I am forever indebted to you and I will never forget the values you have instilled in me throughout my entire life.

Acknowledgements

This work was sponsored by the Federal Aviation Administration, Grant #12-G-011. The collaboration between the Federal Aviation Administration and the Department of Fire Protection Engineering is invaluable and this work is made possible by their support.

Additionally, I would like to acknowledge my advisor Prof. Stanislav Stoliarov for his guidance and support over the past two years. He has taught me that quality work is only obtainable by hard work, and that I should never settle for work that is not truly quality. I am very lucky to have worked with such a knowledgeable, gracious, and patient advisor during my master's degree.

Additional thanks to my committee members, Dr. Marino diMarzo and Dr. Peter Sunderland. Thank you for sharing your time for reviewing this thesis, and for offering continuous knowledge during my undergraduate and graduate studies.

I would like to also acknowledge my groupmates, who have been a tremendous support during my graduate work, and all other Fire Protection Engineering faculty, staff, and students who have become colleagues and friends. You truly make coming to work very easy, and I thank you for all of the support and memories.

Lastly, I would like to thank my family for your continuous love and support, particularly my parents and my brother. You are my foundation and I am very lucky to have such a strong group to support me through my studies and through life.

Table of Contents

Dedication	ii	
Acknowledgements	iii	
Table of Contents	iv	
List of Tables	vi	
List of Figures	vii	
List of Equations	viii	
List of Abbreviations	ix	
Chapter 1: Introduction	1	
1.1 Motivation		1
1.1.1 Radiation and the radiative fraction		1
1.1.2 Laminar flames		3
1.1.3 Polymers and laminar flame studies		4
1.2 Background		4
1.2.1 Various definitions of heat release rate		4
1.2.2 Smoke point definition		6
1.3 Previous studies		7
1.3.1 Radiation measurements of laminar flames of gaseous fuel		8
1.3.2 Radiation measurements of turbulent flames of gaseous fuels		12
1.3.3 Radiation measurements of turbulent flames of solid state fuels		17
1.4 Current approach		21
Chapter 2: Methodology	23	
2.1 Experimental Setup		23
2.1.1 Overview of the Milligram-Scale Flaming Calorimeter (MFC) enclosure		23
2.1.2 Choice of settings and validation		26
2.1.3 Test matrix for current study		31
2.2 Experimental procedure of radiation measurements		33
2.2.1 Testing preparation		33
2.2.2 Gaseous fuel testing method		34
2.2.3 Solid-state fuel testing method		35
2.3 Analysis of radiation measurements		36
2.3.1 Heat flux gauge data averaging and corrections		37
2.3.2 Preliminary image analysis		38
2.3.3 Radius profile and flame height determination		39
2.3.4 Intensity profile determination		43

2.4 Experimental procedure and analysis of total heat release rate measurements	44
2.4.1 Gaseous fuel testing method	46
2.4.2 Solid-state fuel testing method	49
2.5 Calculation of flame-to-gauge heat transfer	50
2.5.1 Establishing geometric considerations	50
2.5.2 Modeling the flame-gauge interaction and acquiring $c(z)$ and $I_f(z)$	55
2.5.3 Calculation of the total flame radiation and the radiative fraction	57
2.5.4 Validation of methodology and MATLAB analysis script	58
2.6 Sensitivity analysis of method	61
2.6.1 Choice of co-flow rate	61
2.6.2 Choice of thresholding value	62
2.6.3 Choice of bandpass filter	63
2.6.4 Flame flickering	64
2.6.5 Radius profile, centerline profile and heat flux gauge measurements	65
2.6.6 Mass flow rate and heat of combustion	66
Chapter 3: Results	67
3.1 Results of radiation measurements	67
3.1.1 Results of radius profile, $R(z)$	67
3.1.2 Results of centerline intensity, $I_c(z)$	69
3.1.3 Results of flame heights, h_f	71
3.1.4 Results of heat flux gauge readings, q''_{gage}	73
3.1.5 Results of relation function, $c(z)$	75
3.1.6 Results of flame radiation intensity, $I_f(z)$	78
3.1.7 Results of total radiation, Q_{rad} .	79
3.2 Results of heat of combustion experiments	81
3.3 Results of total heat release rate and radiative fraction	82
3.3.1 Results of total heat release, Q_{tot}	82
3.3.1 Results of radiative fraction, χ_r	84
3.4 Comparison to literature values	85
3.4.1 Propane and methane flame comparison	85
3.4.2 Acetylene and polyethylene flame comparison	88
3.5 Flame height versus heat release rate	90
Chapter 5: Conclusions and future work	92
5.1 Conclusions	92
5.2 Recommendations for future work	93
Appendices	96
Appendix A: MATLAB Script- Method validation with cone formation	96
Appendix B: MATLAB script- Processing code for calculation of $c(z)$	100
Appendix B: MATLAB script-Processing code for calculation of χ_R	111
Bibliography	114

List of Tables

Table 1. Positions (x_g, z_g) of the heat flux gauge for all gauge heights	31
Table 2. Test matrix for all tests done in this study. The fuel type, camera exposure time setting, fuel flow rate, and the reference gauge height flux are shown.	32
Table 3. Flow conditions for heat of combustion tests.	47
Table 11. Fractional error of measured parameters.	51
Table 4. Analytical versus calculated view factor for validation configurations.	59
Table 5. Radiative fraction for acetylene and methane.....	62
Table 6. Results of h_f , gauge placement and mean q''_{gage} for all experiments.	72
Table 7. Coefficients and curve specifications for relation functions of all flames. ..	75
Table 8. Total radiation Q_{rad} [kW] of all flames.	80
Table 9. Measured heat of combustion values for all fuels..	81
Table 10. Compiled heat of combustion, total radiation loss, and radiative fraction	83

List of Figures

Figure 1. MFC Schematic (Raffan-Montoya, Ding, & Stoliarov).....	24
Figure 2. Full setup with draft hood shown	25
Figure 3. Radiation measurement setup with labels.	25
Figure 4. T-shaped calibration piece.....	29
Figure 5. Spectral range of camera compared with blackbody emission curves.	30
Figure 6. Subset of image taken for processing.....	39
Figure 7. Contour plot of various threshold values for a methane flame.	41
Figure 8. Radius profile determination, shown with methane flame.....	42
Figure 9. Raw intensity profile along the flame axis location.	44
Figure 10. 2-D and 3-D rendering of the axisymmetric flame..	51
Figure 11. Geometry showing two differential objects in space.	54
Figure 12. Spherical setup used in validation of view factor calculations.....	59
Figure 13. Conical setup used in validation of view factor calculations..	60
Figure 14. Flame fluctuations	64
Figure 15. Radius profiles of all fuels.....	68
Figure 16. Centerline camera intensity profiles of all fuels.....	70
Figure 17. Relation function $c(z)$ curves for all fuels and flame heights.....	76
Figure 18. Measured and predicted heat flux gauge values.....	77
Figure 19. Radiation intensity profiles of all fuels	79
Figure 20. Total radiation of flames plotted against the measured flame heights.	80
Figure 21. Measured radiative fractions: high smoke point fuels.....	86
Figure 22. Measured radiative fractions: low smoke point fuels.....	89
Figure 23. Flame height plotted as function of heat release rate.	90

List of Equations

(Eqn. 1)	6
(Eqn. 2)	8
(Eqn. 3)	10
(Eqn. 4)	14
(Eqn. 5)	15
(Eqn. 6)	15
(Eqn. 7)	18
(Eqn. 8)	19
(Eqn. 9)	44
(Eqn. 10)	45
(Eqn. 11)	47
(Eqn. 12)	49
(Eqn. 13)	52
(Eqn. 14)	52
(Eqn. 15)	53
(Eqn. 16)	53
(Eqn. 17)	53
(Eqn. 18)	54
(Eqn. 19)	54
(Eqn. 20)	54
(Eqn. 21)	55
(Eqn. 22)	56
(Eqn. 23)	57
(Eqn. 24)	58
(Eqn. 25)	58
(Eqn. 26)	59
(Eqn. 27)	60
(Eqn. 28)	87

List of Abbreviations

FDS	Fire Dynamics Simulator
FPA	Fire Propagation Apparatus
CO ₂	Carbon dioxide
CO	Carbon monoxide
CDG	Carbon dioxide generation
OC	Oxygen consumption
PMMA	Poly(methyl-methacrylate)
CFD	Computational fluid dynamics
MFC	Milligram-scale flaming calorimeter
DSLR	Digital single-lens reflex
SLPM	Standard liters per minute
SCCM	Standard cubic centimeters per minute
NIST	National Institute of Standards and Technology
LHV	Lower heating value
HHV	Higher heating value
MCC	Microscale Combustion Calorimetry

Chapter 1: Introduction

1.1 Motivation

1.1.1 Radiation and the radiative fraction

The radiation emitted from a flame is a fundamental quantity for predicting the development of a flame and understanding the heat transfer in a fire scenario. Radiation can be the dominant heat transfer mode in fire spread, particularly for large flames where soot is produced in large volumes. One of the most important radiation parameters is the radiative fraction, χ_R , which is the portion of heat that leaves the flame through radiation. The radiative fraction is important because it is a means of quantifying the portion of energy that contributes to a radiant heat flux, which is often responsible for preheating and igniting unburnt fuels in fire scenarios.

Although the radiative fraction is a useful parameter for predicting the development of fire scenarios, the radiant fraction of a particular fuel varies with a change in the fire size (Markstein G. , 1984) or environmental conditions (Sivathanu & Gore, 1994). Within the turbulent regime, the radiative fraction is considered a property of the flame, given that the radiant fraction remains a constant for turbulent flames (Markstein G. , 1984). Markstein shows that within the range of 5-40 kW, the radiative fraction of propane remains constant at $\chi_R=0.280$, and the same holds true for a number of other turbulent diffusion flames of gaseous fuels (Markstein G. , 1984). However, Markstein also explored laminar diffusion flames and found that radiation fraction

varies within the laminar regime, increasing with an increase in total heat release rate (Markstein G. , 1984). This variation brings into question whether the radiative fraction is truly a property of a particular fuel. Various works, including Markstein's, have shown that there is a relationship between the radiative fraction and flame properties, such as total heat release rate or smoke point (Markstein G. , 1984). Therefore, if a fortified relationship can be established between the radiative fraction and a defining property of the flame (such as heat release rate or flame height), the radiative fraction could be treated as a property of a fuel, regardless of whether it is a laminar or turbulent flame.

Understanding the radiation properties of fuels, such as the radiative fraction, is a key step toward accurately predicting flame spread in simplified and complex numerical models. In computational models, such as the Fire Dynamics Simulator (FDS) the radiative fraction is considered “the most important radiation parameter” (McGrattan et al.). Many of the radiation calculations depend upon user input, such as the resolution of the model, which has a large influence on the local species concentration and temperature calculations. This is important because the species concentration and temperature values are fundamental to the radiation transport equation. In models where users do not want to rely on the radiation transport equation for computing radiation loss, users explicitly define the radiative fraction, which is taken at a default value of 0.35 in large eddy simulations of fires (McGrattan et al.). This results in either generalized radiation estimations (when using the 0.35 default value), or a reliance on accurate data for an informed user to put into the model. In many simplified hand-calculations and correlations, the radiative portion of heat

release for large fires is estimated as 30%, with convection dominating the other 70% of heat transfer (Klote). Faulty assumptions or estimations of the radiative fraction can result in noticeable miscalculations of radiative heat release. With the importance of radiation in mind, there must be methods of accurately measuring radiation for various fuel types at various flame sizes and burning conditions.

1.1.2 Laminar flames

In comparing turbulent to laminar flames, laminar flames are a sound choice for studying radiation characteristics because they are void of the complications of turbulence-radiation interactions (as well as turbulence-chemistry interactions) (Sivathanu & Gore, 1994). Thermochemical interactions are still important in laminar flames but can be simpler to quantify due to semi-stable flames and consequently more stable regions of the flame. For short laminar diffusion jet flames with co-flow of an oxidizer, the flames can become nearly stable in space, creating a flame that is ideal for optical measurements due to a low dependence on temporal changes. With these flames it is possible to map properties such as temperature, soot yield, radiation intensity, or flame shape without the complication of a transient flame shape. Additionally, there are potential scaling parameters between laminar and turbulent flames, which could make laminar measurements an economical test that may be extrapolated to various flaming conditions. Therefore, understanding the relationship between laminar and turbulent radiation properties is a key area of study to further develop future research and the predictive capabilities of fire modeling.

1.1.3 Polymers and laminar flame studies

Although a number of studies have been done to understand the radiation from laminar flames, all of these studies have been conducted with gaseous fuels. This is primarily due to an inability to produce steady laminar flames with solid fuels. However, with the growing popularity of polymers in manufactured goods, understanding the fire risk of these materials is of utmost importance. Inherent flammability risks limit the growth and application of polymeric materials, and with a growing number of available polymer mixtures there must be fast and efficient methods of measuring the risks of the materials. Although the radiative properties of polymers have been studied in bench-scale tests such as the fire propagation apparatus (FPA) (Tewarson, Combustion efficiency and its radiative component, 2004) or the cone calorimeter (Quintiere et al.) these tests require a relatively large sample size and require measurements of the convective losses, which is costly and has notable uncertainties associated with the measurements. Additionally, these tests result in turbulent flames, which present complexity in measuring radiation, as discussed in Section 1.1.2. Therefore, developing a method of measuring the radiative properties of small scale, laminar flames of solid fuels is of particular interest, and this study aims to present such a method.

1.2 Background

1.2.1 Various definitions of heat release rate

The radiant component of energy transfer from fires is studied using many methods, varying with the size, type and environment of fires. The heat release from

fires is extensively studied and the corresponding fraction of energy leaving through radiation is an important component of fire dynamics and flame spread. One important parameter for quantifying the heat release is the net heat of combustion. Theoretical complete heats of combustion are found from calculations using the stoichiometric standard combustion equation and the heats of formation for the reactants (fuel), and idealized products (CO₂ and water) (Tewarson, SFPE Handbook). The heat of complete combustion is typically expressed as a theoretical value, given that few combustion processes are truly “complete.” Due to the production of soot, CO, or other bi-products during combustion, incomplete combustion is typical and is described by the net heat of combustion. The net heat of complete combustion is defined as “the calorific energy generated in chemical reactions leading to complete combustion per unit mass of fuel” (Tewarson, SFPE Handbook). Typical ways of experimentally measuring the net heat of complete combustion are using oxygen bomb calorimetry, cone calorimetry, or other calorimetry methods.

A unique definition of the net heat of combustion is the chemical heat of combustion, defined by Tewarson (Tewarson, SFPE Handbook). The chemical heat of combustion is a value describing the net heat of combustion based on the efficiency of the combustion process. The combustion efficiency, or X_{ch} , is defined as a ratio that describes the fraction of the total heat released through chemical reactions, or a ratio of the chemical heat of combustion to the net heat of complete combustion. The value of X_{ch} is consequently used to relate the total heat release rate to the chemical heat release rate (Tewarson, SFPE Handbook). The chemical heat release rate of gaseous and solid fuels can be determined through multiple calorimetry methods, most notably carbon

dioxide generation (CDG) and oxygen consumption (OC) calorimetry. Both methods rely on empirical relationships between the consumption (OC method) or production (CDG) and the amount of energy released. Corrections for incomplete combustion must be accounted for in the calculations of the chemical heat release rate, particularly in under-ventilated or suppressed combustion scenarios (Tewarson, SFPE Handbook).

The chemical heat release rate is composed of two modes of heat release, convective and radiative heat releases. The convective and radiative components of the chemical heat release rate are often described by the convective and radiative fractions, χ_{con} and χ_r . These components sum to be equal to the chemical combustion efficiency, and this relationship is given as

$$\chi_{ch} = \chi_{con} + \chi_r \quad (\text{Eqn. 1})$$

(It should be noted that this definition is specific to the work of Tewarson, and the radiative and convection portions are typically assumed to sum to unity, or the relationship is typically assumed to be $\chi_{con} + \chi_r = 1$ for most other studies.) The balance between χ_{con} and χ_r shifts with the chemical structure of the flame, which is dependent on fuel, fire size, and ventilation conditions (Tewarson, SFPE Handbook). Given this relationship, the radiative component of energy loss is often found inversely by first measuring the convective component.

1.2.2 Smoke point definition

As pointed out in Tewarson's study, the radiative properties of a flame depend on the chemical structure of the flame. The fuel smoke point (L_s) is a parameter recognized for characterizing the relation between flame behavior and the chemical make-up of a fuel. Consequently, multiple studies have characterized the radiative

properties of a flame based on the observation of the smoke point. The SFPE Handbook defines the smoke point as the “maximum height of [the flame’s] laminar flame (or fuel mass flow rate) burning in air at which soot is just released from the flame tip” (Hurley, et al., 2016). Additionally, the smoke point is often defined in terms of the heat release rate at which soot is first released from the flame tip (Hurley, et al., 2016). The smoke point has been a convenient parameter for characterizing soot production and radiation effects in flames of gaseous fuels due to being easily determined (visually) for many gases. At the smoke point, a chamber of soot (smoke) is released through the very tip of the flame and characteristic “wings” become visible just below the tip of the flame. For laminar flames, the smoke point represents the balance between soot formation and soot oxidation in a flame. At the smoke point, the soot produced at the base of the flame begins to escape through the tip of the flame because it is not yet oxidized. This imbalance occurs due to the increased radiative heat loss, which leads to cooling at the flame tip and the consequent lack of energy for oxidation (de Ris & Cheng). This understanding of the smoke point highlights the trend that sootier fuels result in lower critical smoke points, and less-sooty fuels (fuels which burn closer to a “complete combustion” scenario) will approach infinitely high smoke points. This parameter is important to highlight because many researchers have defined methods of radiative fraction measurement of gaseous fuels based on the smoke point.

1.3 Previous studies

Various studies that measured the radiation from flames of laminar and turbulent flames of gaseous fuels, and the turbulent flames of solid fuels. A thorough

review of these studies give insight to important considerations when developing the current method and a pool of data to validate the results of this method against.

1.3.1 Radiation measurements of laminar flames of gaseous fuel

There have been various studies that have measured the radiant fraction of laminar flames of gaseous fuels. These studies have utilized various measurement techniques, including the use of radiometers and cameras.

A study by Markstein (Markstein G. , 1984) studied the relationship between the radiative fraction and the smoke point of laminar diffusion flames of gaseous fuels. Obtaining deeper knowledge of the relationship between radiative emission and the smoke point, particularly for laminar diffusion flames, was the motivation for Markstein's study. In the study, laminar fuel-jet flames were studied with the use of a wide-view-angle radiometer with a thermopile sensor, which was equipped with a shutter and internal apertures to account for stray radiation and was placed 300mm from the burner axis. The radiometer measured the irradiance of a laminar flame 4.1mm diameter thin-walled burner that supplied gaseous fuels. A co-flow of air was provided by a tube of 152mm inner diameter, and the burner was enclosed to aid in the reduction of heat transfer and flow disturbances. The measured irradiance was related to the radiative power through a spherically isotropic emission assumption (assuming the flame as a point source), given as:

$$\dot{Q}_{rad} = 4\pi S^2 H \quad (\text{Eqn. 2})$$

where \dot{Q}_{rad} is the total radiant power, S is the distance between the radiometer and the flame axis, and H is the measured irradiance. The radiative fraction was obtained as a ratio of the measured radiative power to the theoretical heat release rate, $\chi_R =$

\dot{Q}_r/\dot{Q}_{tot} . \dot{Q}_{tot} is a theoretical value determined by calculations from the heats of formation of the reactants and products, rather than empirically like Tewarson's chemical heat release rate. For the laminar flames, the radiative fraction was not constant, but rather increased to the $\frac{1}{2}$ power with the theoretical total heat release rate. By including the smoke point data, a linear relation between the radiative power and the theoretical total heat release rate *at the smoke point* was found. Further, by accounting for the losses to the burner tube, all fuels of a chemical family (i.e. the alkanes, alkenes, etc...) converge on a plot of the total loss fraction at the smoke point per total heat release rate at the smoke point. This study thus shows an important similarity between the smoke-point and the radiative emissions of laminar and turbulent diffusion flames (Markstein G. , 1984) and provides a comprehensive data set of radiative fractions for gaseous fuel laminar flames.

Escudero et al (Escudero & al.) developed a method of estimating the radiative fractions of laminar diffusion flames by using a Schmidt-Boelter heat flux gauge and a 10.9mm diameter burner with a 100mm co-flow of air. The method for calculating χ_r is based on a general assumption of cylindrical isotropy and accounts for variations in radiation along the flame axis. Propane, ethylene and butane were the fuels under consideration. The heat flux gauge was fitted with a 150° angle sapphire window to eliminate convective contributions and was mounted to a stage motor. The heat flux gauge was positioned at a radial distance $R_c = 120\text{mm}$ from the flame axis and the motor allowed the gauge to transverse the flame height from heights of -115mm to 185mm (where zero corresponds to the exit of the burner). Therefore, an incident heat flux profile along the height of the flame, at a prescribed distance R_c could be used to

determine an ideal radiative heat release rate. The total radiative heat loss was computed by assuming a cylindrical emission at each height and integrating over the height of the flame, given by:

$$\dot{Q}_r = 2\pi R_c \int \dot{q}''_r(R_c, z) dz \quad (\text{Eqn. 3})$$

where $\dot{q}''_r(R_c, z)$ is the heat flux reading of the gauge at each height and dz is taken as 0.32mm. The radiative fraction is then found by dividing the radiative heat loss by the chemical heat release rate. The chemical heat release rate was defined as the product of a constant fuel flow rate (1.471 cc/s) and the chemical heat of combustion as defined by oxygen consumption methods (Escudero & al.).

In turbulent flames, the production of soot and the temperature profile of the flame are fundamental parameters for understanding the radiation from the flame. In order to study the interaction between temperature and soot formation/oxidation kinetics in turbulent flames, Sivathanu (Sivathanu & Gore, 1994) decoupled these factors from turbulent kinetics by studying laminar flames. In the study, Sivathanu applied two models, one for soot kinetics and the other for reaction rates, to laminar diffusion acetylene flames. A model that related radiation to soot production was compared to experimental tests that measured mixture fractions and soot volume fractions of flames. The soot volume fractions were measured using laser extinction and tomography and the mixture fractions were determined using gas sampling and chromatography at various locations in the flames. The radiative portion of energy release was calculated based on the soot volume fraction and the local temperature of the flame, and the chemical heat release rate was found using the species concentrations and their heats of formation. The modeling technique was compared to experimental

findings for acetylene flames and found that changes in an assumed radiative fraction made considerable changes in the calculated reaction rate values and the soot volume fractions (Sivathanu & Gore, 1994). This is an important finding considering the global radiative fraction is often assumed as a constant value in computational or simple hand-calculation models. A non-representative radiative fraction used as input could lead to extremely misleading results of radiation and species concentrations.

Computational solvers are valuable tools that aid in understanding and validating phenomena observed in experimental results. Many studies have utilized computational tools to fortify the results found through experiments. Rankin et al. (Rankin, Blunck, & Katta) used computer-generated images to compare images of a laminar diffusion flame captured with infra-red cameras. The infra-red camera was equipped with a narrow band-pass filter centered on $4.38 \mu\text{m}$, with an integration time of 0.4ms and a sampling frequency of 670 Hz . The spectral range of the camera primarily detected the radiation from carbon dioxide gases. The intensity detected by the lens of the camera was estimated by a line-of-sight approximation. Additionally, computational infrared images were produced using the radiative transfer equation and a narrowband radiation model. The model approximated the flame as a series of axisymmetric concentric rings, each ring with a constant temperature and species concentration. The radiative transfer equation was then used to calculate the line of sight radiation received at the camera, with non-scattering and blackbody emission approximations. The spectral limits of the filter were accounted for in the computational images by bounding the integral of the radiative transfer equation to the limits of the narrow-band filter. Agreement between the measured and computed

images was strong, particularly in the middle-region of the flame. Noticeable differences were apparent in the region just above the burner, where the flame stabilized at the base. In the computed images, a high-intensity region extended to the surface of the burner, indicating an “anchor” to the burner surface. In the measured images, this anchor was missing. This discrepancy points to a challenge in the low-sooting regions of the flame that are difficult to capture by a camera due to emission beyond the visible range (Rankin, Blunck, & Katta, 2012). This finding about anchoring or lifting from the burner outlet presents a challenge to consider when comparing camera imaging to radiative measurements, and is introduced in the results of the current study as well.

1.3.2 Radiation measurements of turbulent flames of gaseous fuels

The 1984 work of Markstein also measured the radiation of turbulent flames of gaseous fuels (Markstein G. , 1984). The experimental setup and processing was the same as the laminar measurements with the exception of the burner and the placement of the radiometer. The turbulent flame burner consisted of a 12.7mm diameter nozzle, with no co-flow of air provided. The radiometer was placed at a distance of 3m from the burner axis in order to avoid geometric effects and treat the flame as a spherically-isotropic point-source emitter. For turbulent flames, a linear relationship between radiative fraction and the smoke point length was established, and the radiative fraction was found to be a constant value across all heat release rates (Markstein G. , 1984). This differs from the laminar flames, which have a power-law dependence on the total heat release rate. The finding of a radiative fraction for propane across all heat release rates in the range of 0-40 kW is important for understanding the radiative fraction's

transition from laminar to turbulent conditions. This study indicates that the radiative fraction begins at a low value for small, laminar flames and gradually increases with increasing heat release rate until the flame transitions to turbulent conditions, at which point the radiative fraction plateaus.

The work of Zheng et al (Zheng, Barlow, & Gore) followed a similar method as Rankin by using infrared measurements compared with computational radiation intensities. The intensities of the images and computations were used to find the temperatures at various locations in the flame, and the statistical noise of the measurements were also spatially mapped. This statistical analysis showed greater noise at locations far from the centerline of the flame. This study primarily focused on analyzing the turbulence-radiation interactions, which is an important characteristic in modeling approaches. The study found that the mean spectral radiation intensities maximized near the location corresponding to the flame height. Additionally, the flow conditions (i.e. the Reynolds number) did not have a large effect on the radiation intensities, nor did turbulence largely affect the regions near the flame axis (indicating that using mean properties obtained at the centerline is an appropriate approach) (Zheng, Barlow, & Gore).

An additional method used to measure the radiation from a flame is the multi-emitter method, where the radiance is measured at a single location by accounting for the radiation from a number of radiating regions of the flame. The works of Gore and Faeth (Gore & Faeth, Structure and Spectral Radiation Properties of Turbulent Ethylene/air Diffusion Flames) and Sivathanu and Gore (Sivathanu & Gore, 1993) considered the radiation from turbulent jet diffusion flames by a semi-infinite

cylindrical enclosure estimation. In these studies, a water-cooled heat flux gauge is placed in the plane of the burner outlet, with the normal vector from the gauge face parallel to the burner. The readings of the heat flux gauge were integrated over a semi-infinite cylindrical enclosure surrounding the flames. These heat flux readings were measured at various radial positions (length of gauge placement from the center of the burner) until the gauge readings sufficiently decreased to the lower limit of the gauge (Sivathanu & Gore, 1993). For some flames, the estimations of the radiative loss as a semi-infinite cylinder were not feasible, and a single-point flame treatment with spherical isotropy assumptions were made in order to measure the heat flux at the gauge front, similar to the methods of Markstein (Markstein G. , 1984) above. The value of χ_r is defined in terms of the lower heating value (LHV), or the complete heat of combustion as calculated from the heats of formation of a stoichiometric combustion reaction, assuming water is produced in the gaseous state.

With a value for χ_r determined, the emitted radiated energy from the flame is estimated by a series of relations between the measured radiative heat flux, the gauge placement geometries, the total heat release rate and the radiative fraction. A spatially-dependent parameter, C^* , is used to characterize the relation between these variables, and is given as:

$$C^* = \frac{q_r 4\pi R^2}{Q_f \chi_r} \quad (\text{Eqn. 4})$$

where q_r is the heat flux at the gauge, R is the radial distance from the center of the burner, Q_f is the total heat release rate from the flame and χ_r is the radiative fraction. The heat flux at the gauge, q_r , is found through a multi-ray method, where the weighted sum is multiplied by the heat flux contributions of each region of the flame, similar to

past studies by Jeng and Faeth (Jeng & Faeth). The heat flux contributions from each region of the flame is found by tracing the radiation along a path S from the radiating region and the face of the heat flux gauge. This path, or ray, is divided into homogenous segments, with assumed constant temperatures and soot volume fractions in each segment. The radiation from each segment can be calculated along the radiation path as:

$$E_e(J) = 4 \int \int i_\lambda d\lambda d\varpi = C_0 f_v T^5 \quad (\text{Eqn. 5})$$

where i_λ is the spectral radiation intensity, $d\varpi$ is the differential solid angle of the ray, f_v is the soot volume fraction, T is the local temperature, and C_0 is a constant that accounts from refractive indices of soot and is assumed to be $2.77 \cdot 10^{-7} \text{ kW/m}^3/\text{K}^5$. The intensity emitted by each segment is given by:

$$I_e(J) = \epsilon_p(J) \sigma T(J)^4 / \pi \quad (\text{Eqn. 6})$$

where ϵ_p is the Planck-mean emissivity, and $\sigma T(J)^4$ is the blackbody emissive power. The intensity contributions of each ray are found using a transmittivity summation equation across the ray segments, and finally the equation of radiative heat transfer is integrated over all ray segments to find the ray's contribution to the radiative intensity at the heat flux gauge. This intensity is then multiplied by a weighting factor determined by the fractional area contributed by the ray, determined by the cosine of the angle between the normal to the gauge and the ray; this multiplication then allows for the summation of all rays to give the heat flux at the gauge, q_r . Approximations of the temperature and soot volume fractions are made in order to complete these calculations. This study found that the values of C^* converged for a number of fuels for a large range

of gauge placement locations, showing that radiative measurements at a single detector location can be used to predict radiative losses from a flame (Sivathanu & Gore, 1993).

A similar study was conducted two decades later by Hankinson (Hankinson & Lowesmith) where non-cylindrical flame shapes were considered and a single point source method was used, for both near-field and far-field measurements. The flames were modeled as multi-point solid flames as cylindrical, conical, back-to-back cone and back-to-back ellipsoid shapes. The solid flame shape models are discretized into various elements, and the multi-ray emitter method of Sivathanu was used. This study found that the multi-emitter, single detector method agreed well with the measurements of Sivathanu, and that errors arose for the areas near the base of the flame and that radiation tended to peak at a location $\frac{3}{4}$ of the way along the flame (Hankinson & Lowesmith).

A recent study by White et al. measured the radiative fraction of a turbulent line burner flame using a multi-emitter method. A water-cooled heat flux gauge placed at a distance of 100cm from the centerline measured the radiance of the flame, while a photodiode and photosensor amplifier were placed at a distance of 190cm to measure visible luminous emissions. The images obtained by the photosensor were used to determine a flame shape, where the flame was resolved to an array of 320x240 point sources. Due to the line-fire configuration, the flame was treated as an optically thin array of emitters, and the atmospheric transmissivity was assumed to be unity. Using the angle between the normal face of the gauge and the line of sight ray from the emitting body, the heat flux contribution of each emitter to the gauge was calculated. In a similar manner to Sivathanu and Hankinson, the radiative heat flux was determined

at each heat flux measurement using the recorded images and weighting factors. The radiative fraction was then found as a ratio of the measured radiative heat release to the total (theoretical) heat release, using the theoretical enthalpy of combustion for each fuel. The measured radiative fractions for the turbulent line fires were consistent with previous studies, and the oxygen concentration of the reaction zone was altered to study the effect of sooting and radiation interactions. As hypothesized, the radiative fraction of heat loss increased with an increase in oxygen, as fuel-limited flames resulted in incomplete combustion reactions and therefore higher soot production (White, Link, & Trouve).

1.3.3 Radiation measurements of turbulent flames of solid state fuels

Tewarson et al. studied the conditions affecting the radiative component of heat loss and found that fire size, ventilation and chemical make-up of the flame have an impact. This study measured the radiative component of heat release by first measuring the convective component in the Fire Propagation Apparatus (FPA- ASTM 2058) and then backing out the radiative component with the use of Equation 1. The convective heat release rate was found by measuring the temperature of the exhaust gases in the sampling duct, the corresponding heat capacity of air at the measured gas temperature, and the mass flow rate of the product-air mixture in the sampling duct. Corrections were made to remove the convective contributions of the radiant panels and to account for the heat loss to the walls of the duct. The value of X_{con} was found by multiplying the integrated value of the corrected convective heat release rate for the duration of the experiment by the net heat of complete combustion and normalizing by the integrated

mass loss rate for the duration of the experiment. With χ_{con} known, χ_r was calculated from $\chi_r = \chi_{ch} - \chi_{con}$. Through a series of experiments with various fuel types and the use of data on the net heat of complete combustion, a relationship between the combustion efficiency and its radiative component was established and showed to be valid for a number of fuels. Tewarson indicated that the use of a fixed, global χ_r value is erroneous due to a dependence on the combustion efficiency, which changes with fire size, ventilation and chemical makeup of the flame (Tewarson, 2004). This dependence is a result of his definition of chemical heat release, as given by Equation 1.

A similar method of calculating the radiation fraction of heat release for turbulent flames was recently done by Quintiere et al. (Quintiere, Lyon, & Crowley, 2016) in the cone calorimeter. The radiation heat loss calculation is based on the chemical heat release rate, \dot{Q}_{chem} , and is found by the energy balance:

$$\dot{Q}_r = \dot{Q}_{chem} - (\dot{m}c_p + K)(T - T_H) \quad (\text{Eqn. 7})$$

where \dot{m} is the mass flow rate based on the temperature at the smoke station, c_p is the specific heat of the hot gases, K is a calibrated value that represents the conductance from the hood surface to air due to convection and radiation, and T is the temperature of the gases at the exit. Predictions of the radiative fraction using this method showed promising agreement with the measurements of Tewarson in the FPA (Quintiere, Lyon, & Crowley, 2016).

Further, the use of a radiometer combined with a camera has become a popular method for tracing the radiative properties of flames. Orloff (Orloff, 1981) and Markstein (Markstein G. , 1981) presented radiometry methods that spatially mapped the radiation distribution across a 0.73m diameter turbulent poly(methylmethacrylate)

(PMMA) pool fire. Similar methods were used by Modak (Modak, 1981) to study the radiation of turbulent pool fires, but with simplified assumptions of constant emission properties and radiation temperatures across the flame shape. Modak's study proved to be useful only for smaller, optically-thin flames, and failed in larger, optically thick pool fire experiments (Modak, 1981). This indicates that the method of coupling radiation measurements with other imaging techniques is a strong choice for small, optically-thin laminar flames.

An earlier study (1981) by Markstein used a scanning radiometer, which allowed for spatially-resolved radiation information of turbulent flames of PMMA pool fires without the need of photographic imaging. The experimental apparatus utilized collimated-beam radiometry, and with the aid of electromagnetically deflected mirrors, the radiometer scanned the flame horizontally and vertically. Due to high sampling capacities, the entire flame could be sampled in 10ms, at a repetition rate of 2 scans per second. At each vertical scanning location, 100 horizontal scans were performed, which provided ample data for averaging over the scans. Average radiance distributions along the vertical axis of the flame were determined to be nearly symmetrical and showed peak radiance intensity at the centerline of the flame. Additionally, averaging and integrating the radiance profiles at each height showed a radiant power profile that maximized near the base of the flame and decayed along the height of the flame. Assuming a constant flame temperature of 1400K and using a gray emission-absorption approximation, the average radiance at any horizontal distance from the centerline of the flame could be given by the radiation equation:

$$N(x) = (\sigma T_f^4 / \pi) \{1 - \exp[-D(x)]\} \quad (\text{Eqn. 8})$$

where $N(x)$ is the averaged radiance, T_f is the average flame temperature, and $D(x)$ is the optical depth, which is approximated as the integral of the emission-absorption coefficient of the radiation path due to the gray-body approximation. The absorption coefficient is obtained through an Abel transformation method. Therefore, Markstein's study also gave insight into the absorption coefficient variation throughout the volume of the flame (Markstein G. , 1981).

This study coupled well with Orloff's study, which combined Markstein's pool radiation data with photograph-derived flame contours to further resolve spatial distributions of radiation. In this study, 0.38 and 0.73m PMMA flames were studied with a 35-mm camera that was placed 7 diameters away from the pool and pointed to the centerline of the flame. A group of 25-100 pictures of each flame were averaged and processed to determine an average flame shape. The highly-turbulent flame resulted in a flame profile composed of multiple "flamelets" which were approximated as a stack of emitting disks at each vertical location. This approximation resulted in a vertically-resolved flame profile, $R(z)$. Any flame shape was assigned a profile $R(z)$ and was approximated as an emitting disk with radiative power data taken from the work of Markstein (Markstein G. , 1981). The intensity threshold for determining the edge of the flame was set to one-sixth of the maximum intensity of the photograph, and the resulting profiles agreed well with the radiation-derived contours of Markstein's (1981) study. A radiometer viewing through a horizontal slit measured flame radiant flux along the height of the flame, which allows for the calculation of the approximate flame temperature. This flame temperature was then used in the radiation equation (Eqn. 8) to find the radiant flux at an (x,y) location away from the flame. The radiative

fraction was then found by using an approximation for the mass loss rate from the surface of the pool and the theoretical complete heat of combustion for PMMA. The study found a shift from $\chi_r = 0.32$ to 0.42 for various PMMA pool fire profiles (Orloff, 1981). Although this study focused on turbulent flames, the images techniques are useful for developing the methodology of this study.

1.4 Current approach

Although laminar flames of gaseous fuels and turbulent flames of both gaseous and solid fuels are well-studied, there is void of studies done on the laminar flames of solid-state fuels. This is largely because producing repeatable laminar flames with solid samples is difficult to do experimentally. Additionally, the current studies done on turbulent flames of solid fuels are not ideal because they rely on the measurement of convective heat release, or need measurements of temperature, species concentration, or soot production. The current study's unique methodology presents a method of measuring flame radiation without measuring convective effects or without needing information about the temperature or species production in the flame. The current study measures the spatially-resolved radiation intensity [$\text{kW/m}^2\text{-srad}$] and the radiative fraction for laminar diffusion flames of solid fuels, as well as laminar fuels. With the aid of the novel Milligram-scale Flaming Calorimeter (MFC), 30mg samples of polyethylene (PE) are volatilized in a 12.8mm burner tube and flames are introduced with a co-flow of air. Flames between 2 and 7cm are studied, with total heat release rates ranging from 30 to 150 W. The capabilities of the MFC allow for the measurement of gaseous propane, acetylene, and methane fuels as well.

Similar imaging techniques of White et al. (White, Link, & Trouve) are utilized to capture a series of images of the flame with a Nikon DSLR camera that has been equipped with a 900nm band pass filter. Spatially-dependent radius and intensity profiles are determined from the images. A Schmidt-Boelter thermopile heat flux gauge is used to measure the incident heat flux at radial locations between 3.5-5.0cm.

A relation function that relates the heat flux measurements to the profiles obtained by the images is obtained through optimized inverse modelling, and this relation function allows for the determination of a spatially-dependent radiation intensity profile along the height of the flame. From the radiation intensity profile, the total radiation is found.

In order to find the radiation fraction, the total heat release of the flame is calculated based on additional experiments in the MFC that measure the heat of combustion of the various fuels. Using the heats of combustion and the mass flow rate of the fuels, the total heat release rate is calculated and the radiative fraction is taken as the ratio of the radiative to total heat release.

Given the capabilities of the MFC apparatus, this approach is valid for both gaseous and solid fuels, presenting a cost-effective and relatively simple method for determining the radiative properties of laminar diffusion flames. The study is unique in providing a means of measuring these properties for laminar flames of solid fuels, and is therefore an important contribution to the field. The results of the radiation and total heat release tests will be presented here, as will an analysis of the method's sensitivity to various parameters and the uncertainties accompanying the method. Lastly, the results of the preliminary tests are compared to previous studies.

Chapter 2: Methodology

2.1 Experimental Setup

2.1.1 Overview of the Milligram-Scale Flaming Calorimeter (MFC) enclosure

The experimental setup is an adaption of the Milligram-Scale Flaming Calorimeter (MFC) apparatus, which was developed to allow for the small-scale testing of both gaseous and solid samples. Use of the MFC for this study is desirable because of its calorimetry capabilities and its compatibility with non-intrusive methods of studying the flame. The MFC was first developed to study fundamental combustion properties of fuels using small sample sizes, thus saving time and money for testing materials. The setup of the MFC apparatus includes four main parts, shown in Figure 1. The base of the apparatus is made up of the pyrolyzer, which is encased in a 12.8 mm inner-diameter quartz tube. The pyroprobe consists of a coiled heating element that allows small quartz sample tubes to be placed inside. The pyroprobe has the capability to heat the sample at a constant heating rate, with a theoretical heating rate range from 0.01 °C/s to 999.9 °C/s. Within the realm of the MFC test procedure, realistic heating rates are closer to 1 °C/s to 64 °C/s, and the standard heating rate is chosen as 10 °C/s. Heating of the pyroprobe results in heating and decomposition of the solid samples. The volatilized samples are carried out of the tube by a purge gas before being ignited by an ignition coil placed just above the lip of the quartz tube. The base of the MFC also provides a co-flow of gas to stabilize the flame, with the co-flow passing through a

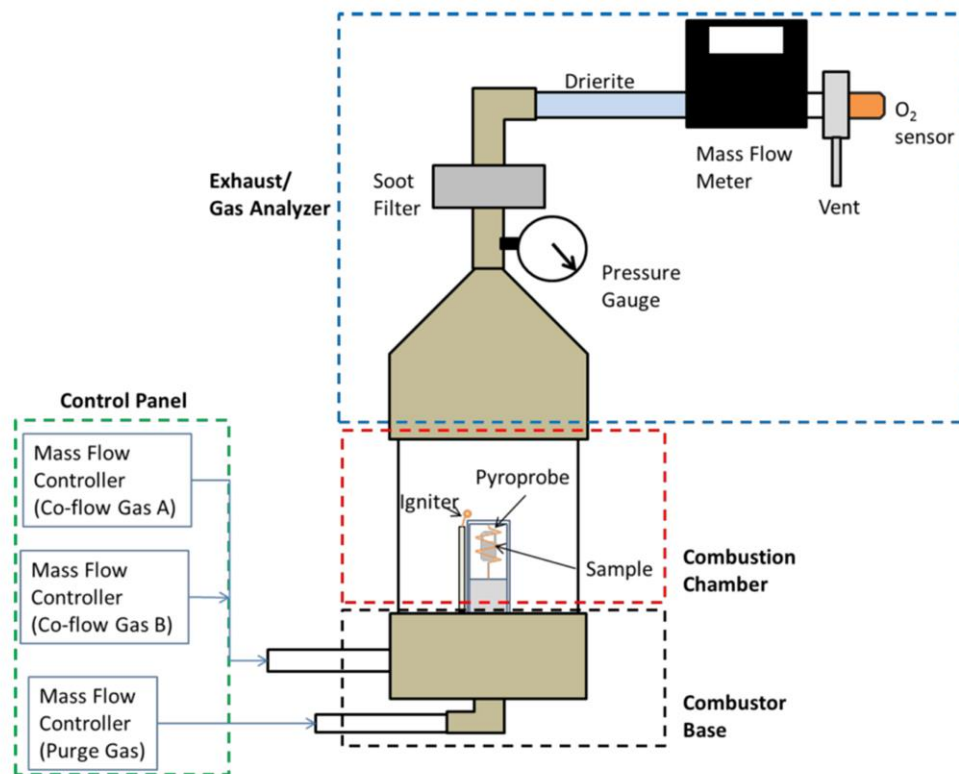


Figure 1. MFC Schematic (Raffan-Montoya, Ding, & Stoliarov)

pool of glass beads to encourage a homogeneous co-flow. The combustion chamber is enclosed by a larger quartz tube (diameter of 70mm) that connects to a brass cone that funnels combustion products and co-flow gases into the gas analyzing system. The gas analyzing system consists of various gas sensors, with an oxygen sensor being of particular importance for oxygen-consumption calorimetry methods. This classic setup of the MFC enclosure is used in this study to obtain the net chemical heats of combustion of all gaseous and solid fuels, as well as the heat release rates for all fuels. For further detailed information on the development and functions of the MFC, please refer to Ding's thesis (Ding).

For the majority of tests done in this study, the MFC enclosure is altered to allow for optical access to the flame, and is shown in Figures 2 and 3. For all dimensions, the origin of the Cartesian coordinate system is at the center of the burner exit. Therefore, $z = 0$ corresponds to the lip of the burner exit (as specified in Figure 3) and $x = 0$ corresponds to the burner's central axis, or the "flame axis". The orientation of the camera in Figure 3 has been rotated by 90° in order to present a 2-dimensional view of the setup; the actual orientation is shown in Figure 2. The enclosure used in this study includes the burner of the MFC apparatus, a shorter quartz co-flow tube (70mm diameter, 4 cm height), a

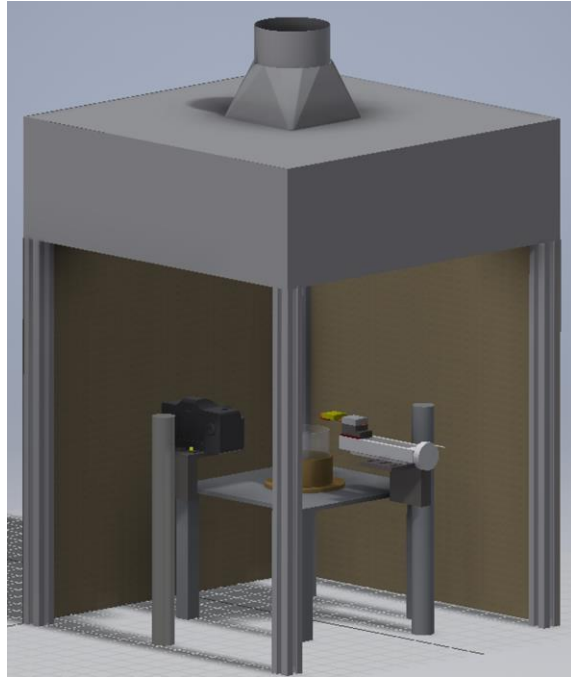


Figure 2. Full setup with draft hood shown

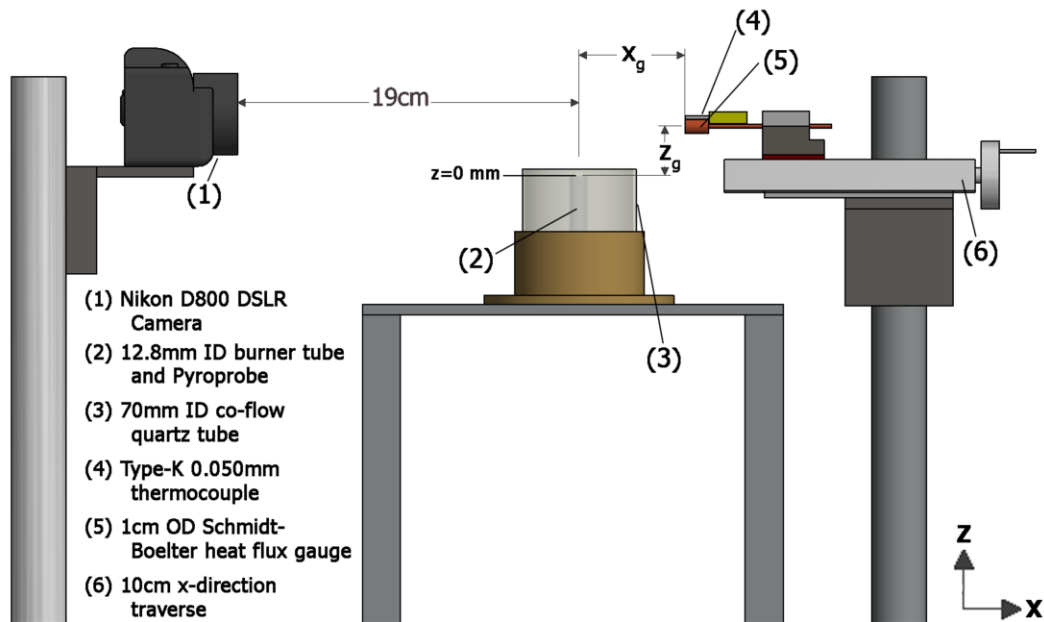


Figure 3. Radiation measurement setup with labels and without the draft hood shown.

Nikon D800 DSLR camera with a 50mm Nikkor Lens, a 1 cm outer-diameter water cooled Schmidt-Boelter heat flux gauge, and an enclosed hood with canvas panels. As shown in Figure 3, a type-K 0.050mm diameter thermocouple is placed directly above the heat flux gauge and the temperature is constantly monitored to detect convective effects that may alter the heat flux gauge readings. An additional thermocouple is placed in the water line that feeds cooled water to the Schmidt-Boelter heat flux gauge. This thermocouple is used to make sure that the water temperature is steady and relatively close to the room temperature. Given that the thermopile of the heat flux gauge uses temperature differences (between the gauge face and the water temperature) to measure the heat flux, maintaining a steady water temperature is important and is therefore closely monitored.

The pyrolyzer and base of the MFC enclosure shown Figure 1 are not altered, but the combustion chamber is altered by the removal of the ignitor and the replacement of the quartz tube with a shorter, 4cm tall tube. The gas analyzing system is removed completely. The camera is placed at a distance of 19cm from the center of the burner, at a height in line with the edge of the burner (the choice of these dimensions are discussed in the next section). The heat flux gauge is positioned in varying locations (x_g, z_g) depending on the height of the flame. The canvas enclosure shown in Figure 2 is composed of an 80-20 frame and canvas panels and is used to conceal the burner from external light and drafts.

2.1.2 Choice of settings and validation

With the use of digital cameras, there are many considerations for choosing the optimal set-up. The sensor of the Nikon D800 DSLR camera used in this study has

been modified through a third party, Max Max LDP, LLC. The alteration of the camera includes replacing the glass provided by the manufacturer with Max Max LDP's custom glass. The alteration extends the sensor's spectrum of detectable wavelengths, which is important for capturing images in the near-IR and IR wavelengths.

In choosing settings for the camera, the author hopes to optimize a tradeoff between high pixel intensity and spatial restraints. One such restraint is the aperture setting, which poses a balance between large aperture (more light allowed in) and appropriate depth of field, since a larger aperture corresponds to a smaller depth of field. The author chooses the smallest f-number (largest aperture) that keeps the front and back of the burner in focus. Additionally, the separation distance between the center of the burner and the position of the camera has a large impact on the depth of field and image greyscale intensities. Therefore, an optimal position is the closest distance to the burner where geometric constraints are not an issue. These constraints include unrepresentative favoring of the front or the back of the flame, which voids the method's assumption of an axisymmetric flame. This constraint is discussed below.

The available settings to change in order to optimize images are (1) the aperture, (2) shutter speed (i.e. exposure time) (3) ISO setting and (4) distance of camera from burner. The aim is to have three of these four factors consistent between all tests and allow the fourth setting to be appropriately changed to match a change in fuel type. Upon optimizing the settings, it was determined that the most appropriate free variable to change between tests is the shutter speed. Therefore, the aperture, ISO setting and distance from the burner are consistent throughout the study. It is desirable to have the fastest shutter speed (slowest exposure time) in order to freeze the flame at a particular

moment in time and to take a quick succession of images. Using a set of two 3D-printed calibration pieces and the DSLR camera, a series of calibration tests allow for optimization of these settings.

The first calibration piece is used to ensure that the camera has the center of the burner set as the focus point of the camera. The calibration piece is a 3D-printed piece that fits snugly on top of the MFC burner and is a cross shape with two perpendicular intersecting planes. With the calibration piece centered and leveled on the burner, the aperture of the camera (which is placed at a given distance from the burner) is opened to the largest aperture. Opening to the largest aperture ensures the narrowest depth of field, allowing for a more precise focusing on the center of the calibration piece. Once the camera is focused at the largest aperture, the aperture is incrementally closed until the depth of field encompasses the entire burner width. For this test, a second calibration piece was used.

The second calibration piece is T-shaped and is also designed to fit snugly on top of the burner. This calibration piece, with a rectangular plane positioned on the edge of the burner rim, allows for testing whether a plane is in the depth of field of the camera. Because the center of the burner is already set as the focal point, the calibration piece can be swiveled to have the plane positioned on the front and back of the burner, thus testing the depth of field. Figure 4 shows the calibration piece positioned on the back (a) and front (b) of the burner. The aim is to have both the front and back positions within the depth of field. If the plane of the calibration piece is not in the depth of field, then the aperture must be closed until the calibration piece comes into focus. The

desired setting for the camera is the largest aperture (smallest f-number) where both the front and back positions are in focus.

The separation distance between the camera lens and the flame axis is of significance, therefore this set of two tests is completed

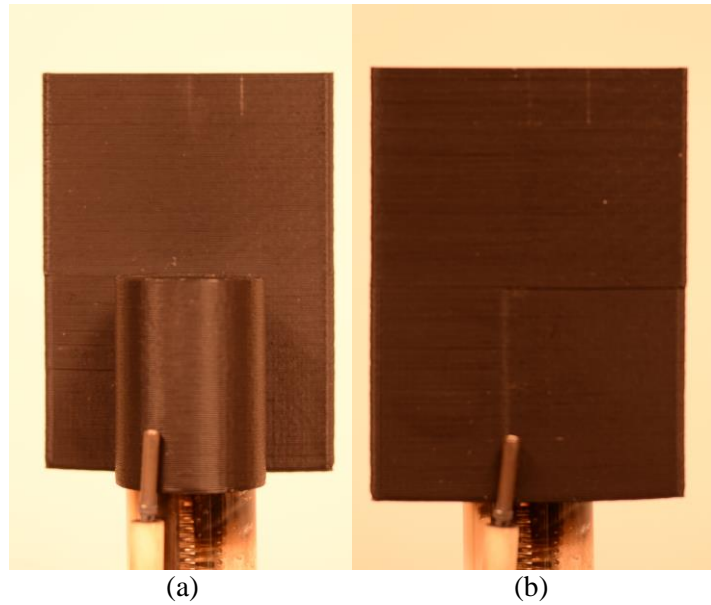


Figure 4. T-shaped calibration piece with plane positioned at the back (a) and the front (b) of the burner.

for various camera placements. This is because the method assumes a symmetric representation of the flame, and therefore the front and back of the burner should occupy similar pixel space. In other words, the T-shaped calibration piece with the rectangular plane placed at the back of the burner should measure a similar pixel length to the piece within the plane at the front of the burner. If the calibration piece in the front position measures much longer than the piece in the back position, then the camera is too close, and geometric effects will contribute to the error of the method. This geometric effect can be quantified by a ratio of the measured pixel length in the front to the measured pixel length in the back. This ratio represents the geometric distortion, and an acceptable ratio is set at 1.1, or a 10% difference in pixel length.

Upon completing the pixel-length test for camera distances varying from 14.5cm to 20.5cm, it is determined that 19cm is the closest distance the camera can be placed without exceeding a 10% pixel length difference. Any distance further than

19cm has a pixel difference ratio less than 10%. Given a strong drop-off in intensity with increased distance from the burner, 19cm is chosen as the best distance for the set-up. With a determined distance, the aperture tests show that the largest aperture that encompassed the entire burner width in the depth of field was an f-stop of f-8, with an ISO of 200 and variable exposure time. These settings remained consistent throughout the duration of this study.

An important consideration is understanding the amount of radiation that can be captured by the camera, based on the limitations of the camera's sensor. The camera has been altered to allow for an extended spectral range of 360-1100nm. Figure 5 shows the camera's range against the blackbody spectral emission for blackbody emitters at various

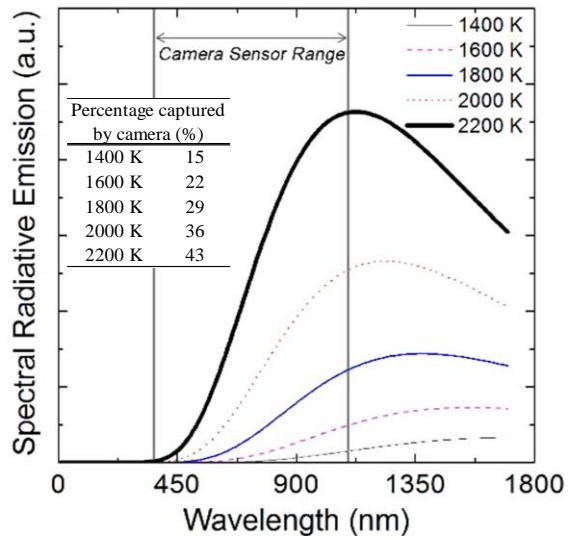


Figure 5. Spectral range of camera compared with blackbody emission curve at various temperatures (Goulay).

temperatures (Goulay), which is representative of idealized soot emission. This shows that in the range of 1400-1800K, the majority of the radiation emitted by the flame and captured by the camera is in the near IR wavelengths between 800-1100nm. This study aided in deciding the appropriate filter to capture the largest amount of soot radiation.

Taking the information above into consideration, a 900nm filter is chosen to be equipped on the front of the camera's lens. A wavelength of 900nm (± 10 nm) was chosen due to this value being in the infrared region where soot emission dominates,

while not being too close to the edge of the camera’s sensor range, which maximizes at 1100nm but becomes insensitive near the edge of this range.

2.1.3 Test matrix for current study

In the current study, one solid fuel and three gaseous fuels are studied. Polyethylene (PE) is chosen as the solid fuel, due to it being a non-charring polymer that burns steadily in the MFC apparatus. Experimental grade pure propane, methane and acetylene are the gaseous fuels

Table 1. Positions (x_g, z_g) of the heat flux gauge for all gauge heights

x_g (cm)	z_g (cm)
3.5	0.9
3.9	1.5
4.2	2.5
4.6	3.5
5.2	4.9

used in the study, which are used to validate the method due to various literature values being available for radiative fraction of these gaseous fuels. For each fuel, three flame heights (two for polyethylene) are studied, and the heat flux at each flame height is measured at a minimum of three different heat flux gauge positions. For each case shown (specific fuel, fuel flow rate, and gauge position), three trials are done in order to understand the accuracy of the measurements. Therefore, there are a total of 33 trials done in this study. The (x_g, z_g) locations of the gauge positions are further specified in Table 1. The particular fuel flow rates were chosen in order to produce a set of flames with flame height varying from 2-6 centimeters. The heights of 2-6cm corresponds to the typical flame height of solid-state fuels studied in the MFC apparatus, which are the primary concern of this study. The complete test matrix of this study is shown in Table 2.

Table 2. Test matrix for all tests done in this study. The fuel type, camera exposure time setting, fuel flow rate, and the reference gauge height flux are shown.

Fuel	Exposure Time (s)	Conditions (sccm/heating rate)	Gage Ht (cm)		
Propane	1/40	56.0	1.5		
			2.5		
			3.5		
		69.6	1.5		
			3.5		
			4.9		
	106.0	2.5	3.5		
			4.9		
			1.4		
		191.3	2.4	3.4	
				4.9	
				0.9	
Methane	1/1.3		205.0	1.4	
				2.4	
				3.4	
		216.0	5.0		
			1.4		
			2.4		
Acetylene	1/80	94.8	3.4		
			4.9		
			0.9		
		117.8	1.4		
			2.4		
			4.9		
	179.8	0.9	1.4		
			2.4		
			3.4		
		Polyethylene	1/50	8.0 °C/s	4.9
					0.9
					1.4
15.5 °C/s	1.9				
	1.5				
	3.4				
			5.0		

2.2 Experimental procedure of radiation measurements

The experimental method was chosen to be as simple and repeatable as possible and will be outlined here. There are two experimental methods used: one pertaining to the testing of gaseous fuels, and the other for solid fuels. The differences between these two methods are minor but are explained in detail in this section.

2.2.1 Testing preparation

For both the gaseous and solid fuels, testing begins with a spatial calibration of the camera positioning and settings. As mentioned previously, the camera is placed on a mount with the lens 19cm from the center of the burner. With the camera set to an ISO value of 200, the T-shaped calibration piece is placed on the burner and the aperture is opened up completely to f-1.8. Opening the aperture results in the smallest field of view while focusing, ensuring that the focal point is centered on the burner. Once the lens is manually focused on the calibration piece, the aperture is closed until the prescribed aperture of f-8. At this point, all camera settings are in place with the exception of the shutter speed, which is varied amongst tests. A number of photos are taken in ambient conditions with the calibration piece in place for spatial calibration (pixel-to-millimeter conversion factor and pixel location of the center of the burner). The position of the gauge is then set; a cross-angle laser that has been aligned with the center of the burner is turned on, tracing a line-of-sight through the center of the burner. At the prescribed gauge height (gauge height placement varied depending on the test; see Section 2.1.3 for information on gauge placement), the face of the gauge is positioned such that the laser passes directly through the center of the gauge. The calibration piece is then removed and a number of pictures of the set-up are taken (to

capture the pixel location of the burner height and the gauge location). After the acquisition of all calibration images, a 900nm band pass filter is placed on the camera, the shutter speed is set to the prescribed setting, and background images are acquired.

Images of the flame during testing are acquired with the assistance of Triggertrap TC-DC0, a free application for smart phones that allows images to be captured remotely at precise timing without the need of a human trigger. A connection cable connects the camera to a smart phone. The cable extends to the exterior of the enclosure, ensuring a completely enclosed testing environment.

2.2.2 Gaseous fuel testing method

The water for the water-cooled Schmidt-Boelter heat flux gauge is started and allowed to flow for at least 20 minutes prior to the start of data acquisition in order to reach a steady water temperature that is in near-equilibrium with the room temperature. A co-flow of 1.8 SLPM of air is set and the lights are turned off. Background readings of the water temperature, enclosure temperature and heat flux measurements are acquired for one minute for the purpose of monitoring and background removal.

With the lights of the laboratory turned off and the co-flow of air set to 1.8 SLPM, the flow controller of the gaseous fuel is set to the desired flow rate, and a pilot flame is introduced above the burner until a steady flame is established. The pilot flame is removed and the panel of the enclosure is shut to completely enclose the flame. After a few seconds of allowing the flame to stabilize, the data acquisition and image acquisition programs are started at the same time. Sixteen photos are acquired of the flame over a period of 4.8 seconds (images taken at a frequency of 3 Hz), and the fuel flow controller is immediately shut off to end the flame at the same time the final image

is taken. Heat flux gauge data is acquired for an additional 30 seconds after the termination of the flame. The number of images per trial is chosen to be 16 due to the queuing capacity of the Nikon D800 DLSR camera when acquiring RAW 16-bit images. The air co-flow is left on for five minutes between trials to aid in the cooling of the set-up and to ensure the enclosure meets an equilibrium state.

2.2.3 Solid-state fuel testing method

The tests for the solid fuels are very similar, with the exception of the ignition process. Solid fuel samples are placed inside the quartz-tube/pyroprobe tube with the co-flow of air set to 1.8 slpm and a purge gas of pure nitrogen flowing through the burner tube at 50sccm. The CDS 5000 Pyroprobe was prescribed to a particular heating rate based on the desired flame height of 2-6cm, and a lighter was used as a pilot flame. Once a visible flame is established, typically 4-6 seconds after ignition, the pilot flame is removed, the enclosure is closed and image and data acquisition is started.

Due to the additional heat generated by the pyroprobe heating coil, an aluminum radiation shield is added to the exterior of the burner tube in order to block radiation from the coil. The addition of this shield is needed to avoid the heat flux measurements including contributions from the coil. In order to thoroughly remove any radiation contributions from the coil, “background” tests are completed before each set of experiment. These tests included measuring the heat flux contribution of coil, with the aluminum shield on, without a sample in the burner tube. The heat flux gauge measurements are record the incident heat flux during the complete cycle of the pyroprobe. This background heat flux is then subtracted from the heat flux gauge measurements of the radiation tests, ensuring the heat flux is strictly from the flame.

2.3 Analysis of radiation measurements

The methodology used to calculate the radiative fraction and the radiation intensity requires three important inputs from the radiation experiments: a mean heat flux gauge reading \dot{q}''_{gauge} , a radius profile that represents the axisymmetric profile of the flame shape, $R(z)$, and a centerline intensity profile $I_c(z)$. These three parameters are obtained directly from the test data. The heat flux gauge data from the three trials is averaged and background noise is removed to obtain a corrected mean heat flux reading. The images of the three trials are used to obtain radius and intensity profiles and these profiles are averaged over all trials to obtain a mean axisymmetric flame shape and a mean centerline intensity. The method of obtaining these parameters is described below.

The raw data acquired during testing includes the calibration images, the 16 RAW images from each trial, and the DAQ results from each trial. The DAQ results include the data of the thermocouple of the heat flux water line, the thermocouple at the heat flux gage, and heat flux gauge. The data is acquired at a frequency of 6 Hz. The images in RAW format are converted to TIFF formatted files using a program “dcrw” created by D. Coffin. The capabilities of dcrw avoid gamma corrections and result in TIFF images with three (RGB) 16-bit color planes.

The calibration images are first examined to determine the important spatial consideration of the setup, namely the pixel locations of the center of the burner, the top of the burner, the gauge position, and the pixel-to-millimeter conversion; this conversion factor is obtained by dividing the pixel length of the calibration piece by its caliper-measured length of 18.5mm. These parameters are found by eye using digital

displays of the images in MATLAB and the pointer tool, which specifies the pixel location of the pointer.

2.3.1 Heat flux gauge data averaging and corrections

The acquired data of the heat flux gauge are analyzed and averaged over the time period of image acquisition. A representative heat flux curve is shown in Figure 6. The time of acquisition is precisely known based on the exposure time and the number of images acquired, thus the

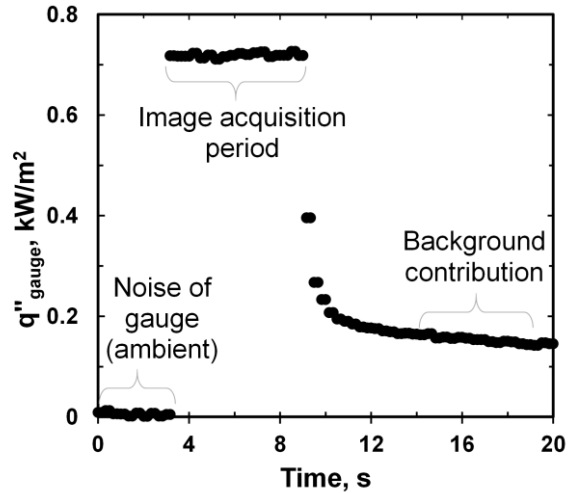


Figure 6. Representative heat flux gauge data for a 4cm propane flame.

corresponding heat flux gauge data is averaged over this acquisition period. As described in Section 2.1.3, three trials are performed at each case (particular fuel, flow rate, and gauge position). A “mean” heat flux reading is obtained by averaging the data points pertaining to the 4.8 seconds of image acquisition of each trial; 2-standard deviations of the mean is recorded as the uncertainty in the measurement.

The heat flux gauge reading is averaged for the 5 seconds after the extinction of the flame to determine a background contribution from the heated apparatus (as seen in Figure 6). The background is taken after the extinction of the flame in order to account for not only the noise of the heat flux gauge, but also contributions from the heated burner tube or an increase in environmental temperatures. The thirty data points pertaining to the 5 seconds of data after extinction of the flame are taken from each trial and then averaged to obtain a “mean” background reading for each test. The mean

background reading is then subtracted from the mean heat flux reading to obtain the corrected mean heat flux gauge reading. This value is treated as the true heat flux reading, or \dot{q}''_{gauge} [kW/m²]. As can be seen in Figure 6, the noise of the heat flux gauge measurements is not large. Before introducing the flame, the gauge reading is near zero (0.02 kW/m²).

2.3.2 Preliminary image analysis

A MATLAB code for processing images is used to acquire the radius and intensity profiles presented below (code provided in Appendix B). In order to determine the radius and intensity profiles, the required inputs for the MATLAB processing tool are the set of images (in .tif format), the exposure time of the camera used to take the images, and the spatial calibration parameters that are discussed in Section 2.2.1; these parameters are the pixel locations of the center of the image, the top of the burner, the gauge location, the pixel-to-millimeter conversion of the images.

In the processing method, all 48 of the images (16 images from 3 separate trials) are analyzed separately to obtain a corresponding (1) radius profile and (2) intensity profile of the flame. After all images are processed, averaging of the profiles occurs. The images are first read using the “imread” function of MATLAB, and the images are then trimmed down to a subset of the image to aid with computational efficiency. This “sub-image” is shown in Figure 7 and is taken from the center of the image to 600 pixels to the right or left of center, and from the top of the image to the top of the burner. This area ensures adequate black space around the flame and is collected for both the right and left sides of the flame.

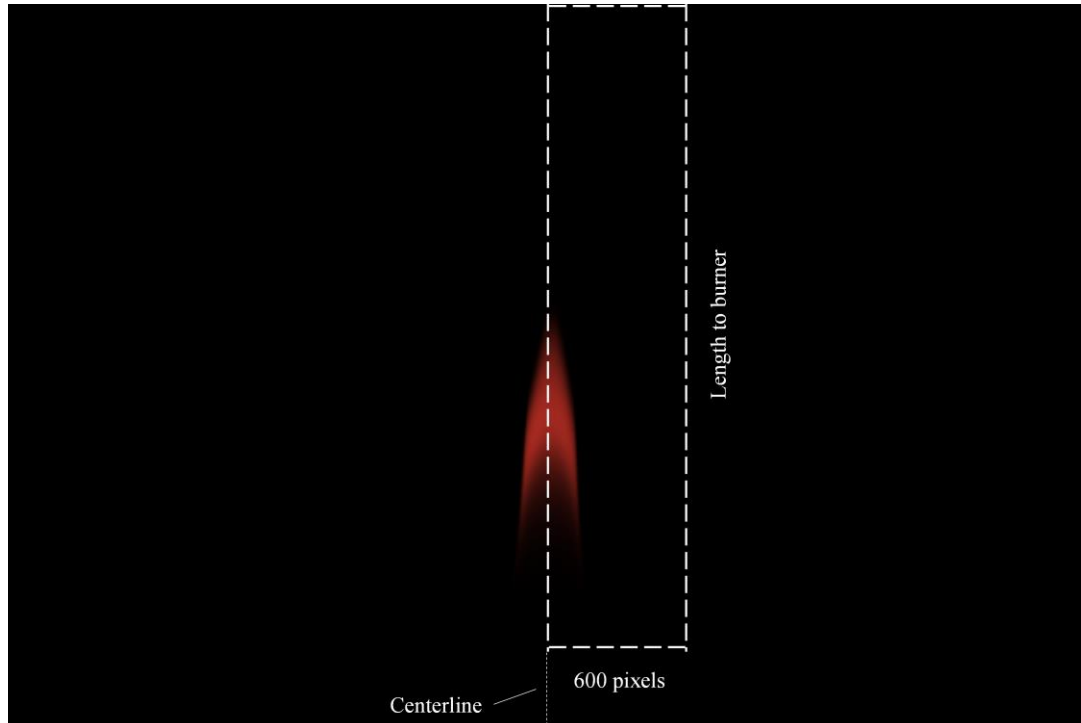


Figure 7. Subset of image taken for processing.

This sub-image is then converted to greyscale by averaging the three RGB channels of each pixel, resulting in a single 16-bit greyscale value for each pixel. The image is finally normalized by the maximum tonal value per channel per pixel for 16-bit images of 65535 to scale the image pixels between values of 0 and 1. The greyscale sub-images (left and right side) of each image are then normalized by the shutter speed to account for the exposure time of each image. Because different exposure times are used to account for the luminosity of the flames, normalizing by the exposure time allows for a meaningful comparison of pixel intensity between fuels.

2.3.3 Radius profile and flame height determination

Next, the radius profiles of the flames for all greyscale images are determined. This profile represents the 2-dimensional contour of the half of the axisymmetric flame that is considered in the sub-image. In order to define the edge of the flame, a threshold

must be set that defines what greyscale value corresponds to a flame region versus a background region. This method defines the threshold using a percentage of the maximum greyscale value detected in the image. This is a similar method of defining the flame shape as Orloff (Orloff), who finds the flame shape using a photomultiplier and defines the flame shape by only accepting regions of the image that have a luminous intensity greater than the luminous intensity of an illuminated screen placed below the flame. This screen acts as a “threshold” value of luminosity (set equal to one-sixth of the maximum luminous intensity of the fire). A benefit of this method, as discussed by Orloff, is that the shape is defined by the threshold setting rather than by camera exposure and settings, which change (Orloff).

When choosing a criterion for defining the flame region, an appropriate threshold value should be stringent enough to be restrained to the flame region but not too stringent, to avoid truncating the low-emission regions of the flame. The best choice is the lowest threshold value (lowest percentage of the maximum pixel value) that clearly defines the flame shape, without being low enough to accept pixels far from the visible flame edge. Additionally, an important region of the flame to study in order to determine appropriate threshold values is the tip of the flame, since this falls at the centerline and defines the height of the flame. The flame tip detected by the chosen threshold criteria should not be strongly dependent on flickering of the flame. The

importance of this criteria can be seen in Figure 8, which shows the contours of various threshold cutoffs (RGB image is shown for clarity- in processing code the greyscale image is used). As can be seen, by setting an overly stringent threshold of 30%, the flame region is constrained to only the strongly visible region of the methane flame shown. However, the 1% and 3% thresholds are too generous, allowing the intensities detected from hot gases to be included (see the deviant behavior at the tip of the flame). Therefore, a stringent yet appropriate threshold was chosen to be any pixels at or above 7% of the maximum pixel value. This value was chosen based on the criteria discussed above, taking into consideration all fuels. The detected flame height does not vary my more than 10% of the flame height in the range of threshold values from 3% to 20%, indicating that the flame height is not largely dependent on this choice.

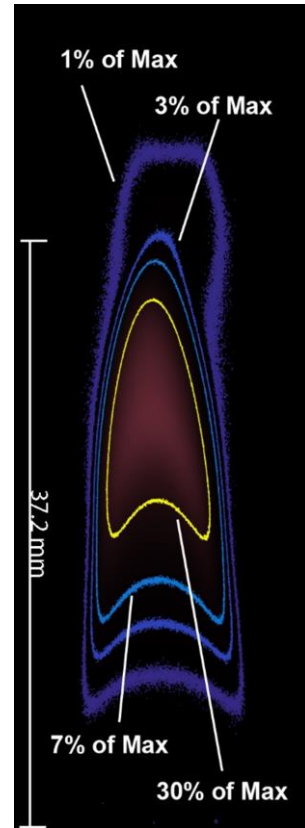


Figure 8. Contour plot of various threshold values for a methane flame.

Using this definition, a threshold value is set to be 7% of the maximum greyscale value in the image. Any pixels with a greyscale value greater than or equal to 7% of the maximum greyscale value of the image are considered to be within the “flame region” and everything below is treated as background.

With the threshold value set, all pixels with a greyscale value equal or greater to 7% of the maximum pixel value are considered to be part of the flame. The outermost pixels that meet the threshold criteria are deemed as the “edge” of the flame, as shown in Figure 9(a). Large gradients in the radius profile are avoided by removing any locations that differ from neighboring points by more than 10%. The detected edge is then fit with a 6th order polynomial using the “fit” function of MATLAB. This polynomial, $R(z)$, is then treated as the radial profile moving forward, as seen in Figure 9(b) for a methane flame. This profile is calculated for both the right and left side of the flame (right and left side of the centerline) resulting in two radius profiles per image. With a set of 144 images per flame height (16 per trial, 3 trials per heat flux gauge placement, and 3 gauge placements) and two profiles per image, 288 radius profiles are compiled per flame height. All of these radius profiles are averaged to find a mean radius profile and the uncertainty is taken as 2-standard deviations of the mean.

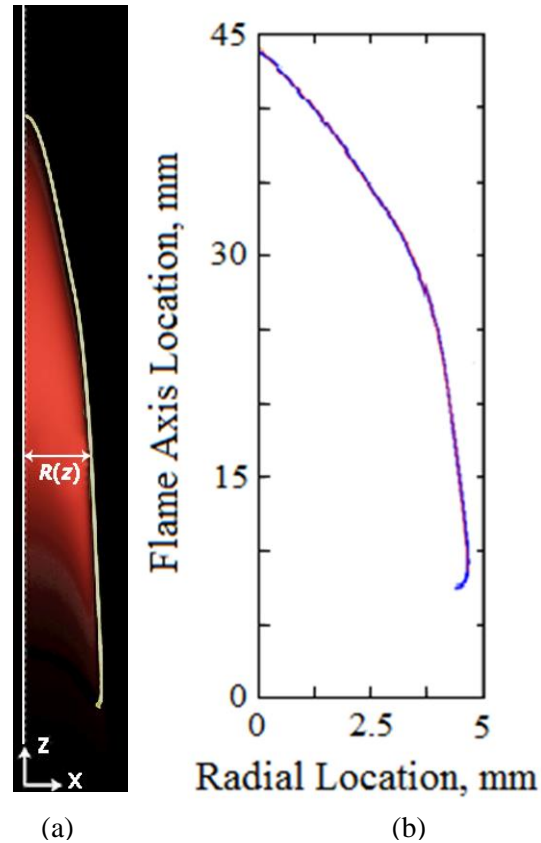


Figure 9. Radius profile determination, shown with methane flame.

10%. The detected edge is then fit with a 6th order polynomial using the “fit” function of MATLAB. This polynomial, $R(z)$, is then treated as the radial profile moving forward, as seen in Figure 9(b) for a methane flame. This profile is calculated for both the right and left side of the flame (right and left side of the centerline) resulting in two radius profiles per image. With a set of 144 images per flame height (16 per trial, 3 trials per heat flux gauge placement, and 3 gauge placements) and two profiles per image, 288 radius profiles are compiled per flame height. All of these radius profiles are averaged to find a mean radius profile and the uncertainty is taken as 2-standard deviations of the mean.

With the radius profile known, the flame height h_f of each flame is found. The threshold value of 7% is a useful parameter for determining where the flame region ends with regards to the flame tip. For each image, the image is scanned to find all pixels in the image that carry a greyscale value greater than 7% of the maximum greyscale value, and these pixels are treated as the “flame region”. Once the flame region is known, the tallest z-location (furthest z-value from the burner exit) can be found and is representative of the z-location where the flame no longer exists; in other words, this is a definition of the flame height. This value is stored for all images of the flames and the flame height values of all 288 half-images are averaged to find a “mean” flame height. This mean flame height is what is used throughout the study as the flame height h_f and is the most accurate depiction of the flame tip. It is especially useful because it remains consistent between flames below the smoke point and flames beyond the smoke point. Because the flame height is determined based on centerline intensity values, rather than a geometric definition of the “tip” of the flame, the flame height can be determined for the flames above the smoke point, which do not have a well-defined tip. The uncertainty of the flame height is taken as two standard deviations of this mean flame height.

2.3.4 Intensity profile determination

In addition to the radial profile, the intensity profile along the flame centerline (along the z axis coming out of the burner) is recorded. The centerline intensity is used as the representative intensity of any radiating element at that given flame axis location (z-location), based on the centerline being the only true line-of-sight locations in the flame. The raw camera “intensity” is taken as the grey-scale 16-bit value of the pixels

along the centerline, after normalization as described in Section 2.3.2, and is therefore in normalized camera units of [1/s]. The centerline intensity values are then fit with a 1st order Gaussian symbolic function using MATLAB’s “fit” function. A representative raw centerline intensity profile with raw data and the corresponding Gaussian fit, $I_c(z)$, is shown in Figure 10 for a propane flame. One intensity profile is found per image, and with 144 images per flame height, the final intensity profile is the average of the 144 profiles. The uncertainty is taken as two-standard deviations of the mean.

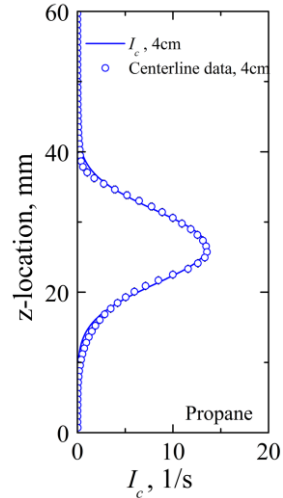


Figure 10. Raw intensity profile along the flame axis location. Symbols represent raw data, solid line is the Gaussian curve fit.

2.4 Experimental procedure and analysis of total heat release rate measurements

The total heat release rate (HRR) is needed in order to find the radiative fraction and is measured with a separate set of experiments. The total heat release rate is defined as:

$$\dot{Q}_{tot} = \dot{m}\Delta h_c \quad (\text{Eqn. 9})$$

where \dot{m} is the mass flow rate of the fuel and Δh_c is the heat of combustion of the fuel. Therefore, the mass flow rate of the fuel and the heat of combustion are found. There are many definitions of the heat of combustion. Due to the variations in the definition of heat of combustion, there is wide-spread variation in the total heat release and accompanying radiative fraction in the literature. One such definition is the complete heat of combustion, which is based on a derivation from the heats of formation of a stoichiometric combustion reaction. The complete heat of combustion is obtained from

calculations involving the heats of formation for the products and reactants of a stoichiometric combustion reaction. The calculation for finding this value is:

$$\Delta h_{c,tot} = \sum(n\Delta H_f^\circ)_{prod} - \sum(n\Delta H_f^\circ)_{react} \quad (\text{Eqn. 10})$$

where n is the number of moles of the product or reactant species in a stoichiometric reaction, ΔH_f° is the heat of formation of the species, “*prod*” specifies a product and “*react*” specifies a reactant. Again, stoichiometric conditions are assumed and carbon dioxide and gaseous water are taken as the only products, with just the fuel and oxygen as the reactants. This definition of Δh_c is synonymous to the lower heating value (LHV) definition of Turns (Turns).

Another definition is the chemical heat of combustion which is determined using the net heat of complete combustion per unit mass of oxygen consumed, ΔH_O^* . This net heat of complete combustion per mass of oxygen is an empirically derived value and varies depending on the fuel; values of ΔH_O^* are provided by Tewarson (Tewarson, SFPE Handbook). The chemical heat of combustion is distinct from the complete heat of combustion due to it accounting for the effects of incomplete combustion. Due to the production of soot, CO, or other bi-products during combustion, incomplete combustion is typical and is described by the chemical heat of combustion. The chemical heat of combustion describes the net heat of combustion based on the efficiency of the combustion process. The combustion efficiency, or X_{ch} , is a ratio that describes the fraction of the total heat released through chemical reactions, or a ratio of the chemical heat of combustion to the net heat of complete combustion. The value of X_{ch} is consequently an important parameter and closely related to the chemical heat release rate (Tewarson, SFPE Handbook).

In order to avoid using a heat of combustion that does not appropriately define the heat release in the setup of the MFC, the heat of combustion is directly measured using the oxygen-consumption capabilities of the MFC. The procedure for measuring the heat of combustion follow the standard method for using the MFC as specified by Ding (Ding) and Raffan (Raffan-Montoya, Ding, & Stoliarov) with a few alterations. The measured heats of combustion are compared to complete heats of combustion that are computed with Eqn. 10.

2.4.1 Gaseous fuel testing method

The mass flow of fuel into the system is explicitly known for gaseous fuels due to the use of a digital volumetric flow meter. With the volumetric flow rate of the fuel known (\dot{V}_f), the mass flow rate can be found by multiplying \dot{V}_f by the density of the gas at standard conditions of 25°C and 1atm.

The heat of combustion tests for the gaseous fuels deviate from the standard procedure of (Ding) due to the MFC being designed for solid fuel samples. Because the fuel is supplied at an infinite and constant rate, rather than a finite and transient rate, the typical procedure of the MFC would lead to an oversaturation of the soot filter or Drierite put into place to protect the oxygen sensor. Therefore, the test is limited to a duration of 30 seconds, at which point the mass flow to the enclosure was stopped. Before each test, with the co-flow of air running through the enclosed system, data is acquired for 30 seconds to obtain a steady-steady reading, which is used as the “flow in” data in the calculation. After the steady state data is acquired, the flame system is opened, the flame is ignited with a pilot flame from a lighter, and the mass flow is allowed to steady before enclosing the system and beginning data acquisition.

The co-flow of air is altered in order to obtain appropriate changes in oxygen concentration due to excessive drops in oxygen choking the flame, causing physical changes in the flame. In order to determine

Table 3. Flow conditions for heat of combustion tests.

Fuel	\dot{V}_{fuel} , sccm	\dot{V}_{air} , slpm
Propane	55.68	5.14
	69.20	5.16
Methane	203.83	6.10
Acetylene	94.26	4.91

the appropriate co-flow rate, a flame is introduced and the co-flow is increased until the oxygen concentration was greater than 15% during steady state burning. The flow conditions for each fuel are shown in Table 3.

The instantaneous heats release rates for gaseous fuel flames were calculated according to “method A” from (Raffan-Montoya, Ding, & Stoliarov), which calculates the heat release rate as:

$$\begin{aligned}
 HRR &= E\Delta\dot{m}_{O_2} = E(\dot{m}_{O_2,in} - \dot{m}_{O_2,out}) \\
 &= E(\rho_{O_2}\dot{V}_{in}[O_2]_{in} - \rho_{O_2}\dot{V}_{out}[O_2]_{out}) \quad (\text{Eqn. 11})
 \end{aligned}$$

where E is an empirically derived heat of combustion of oxygen taken as 13.1 ± 0.6 kJ/g, $\dot{m}_{O_2,in}$ is the mass flow of oxygen into the MFC, $\dot{m}_{O_2,out}$ is the mass flow of oxygen out of the system, ρ_{O_2} is the density of oxygen at standard conditions of 25°C and 1atm, \dot{V}_{in} is the instantaneous flow rate into the system as measured by the flow meters before combustion occurs, \dot{V}_{out} is the instantaneous flow rate out measured by the flow meter, $[O_2]_{in}$ is the oxygen concentration without combustion, and $[O_2]_{out}$ is the instantaneous oxygen concentration as measured by the oxygen sensor of the MFC. One alteration to the method specified by (Raffan-Montoya, Ding, & Stoliarov) that is unique to this study is correcting \dot{V}_{out} by accounting for the makeup of the outflow gases, rather than treating the flow as strictly air. The Alicat Scientific digital flow

meters used in the MFC require a gas to be specified before measuring the volumetric flow. The gas must be specified because the flow meter utilizes pressure difference calculations based on the viscosity of the specified gas to find the flow rates. Because the makeup of the outflow gas is transient and is composed of various gaseous products, the outflow gas is typically estimated as air at the measured pressure and temperature. However, by estimating this flow as air, errors in the flow rate are introduced due to viscous differences in the actual gas flowing through the flow meter. In reality, there is a considerable amount of CO₂ produced in the MFC that flows through the outlet. Accounting for this concentration of CO₂ is an important consideration because the absolute viscosity of CO₂ at standard conditions differs from air by roughly 20%. Therefore, the volumetric flow rate measured by the flow meter was corrected for the actual gaseous makeup by using stoichiometric ratios of reactants and products. Knowing the amount of fuel entering the system, the concentrations and amounts of products of a stoichiometric reaction (CO₂, N₂, H₂O) can be estimated, and the flow is corrected by a ratio of viscosities. This correction makes small differences in the flow rate (~0.5%) but due to the heat of combustion's strong dependence on the volumetric flow rate, it makes noticeable differences in the final heat of combustion values.

The instantaneous heat release rate is found at every time during the 30 second test, resulting in a heat release rate curve that is time dependent. Finally, the total heat release [kJ] is found by integrating the instantaneous heat release rate over the duration of the 30 test. This value is divided by the total mass of fuel burned during the test to get the heat of combustion [kJ/g], following Eqn. 11. The total mass burned is found

by multiplying the mass flow rate by the duration of the test (30 s). This method (Method A) is preferable for gaseous fuels due to the steady dynamics of the test.

2.4.2 Solid-state fuel testing method

The solid fuel tests for polyethylene are conducted according to the MFC's standard procedure, following the specifications of Ding (Ding). The only deviation from the standard procedure is a decrease of co-flow of air from 4slpm to 3slpm and a change in the heating rate of the sample in order to meet the conditions of the tests. The tests are conducted for both the 3.5cm (8°C/s) and 4.5cm (15.5°C/s) flames. The instantaneous heats release rates are calculated according to "method B" from (Raffan-Montoya, Ding, & Stoliarov), which calculates the heat of combustion as:

$$HRR = E\Delta\dot{m}_{O_2} = E \left(\rho_{O_2} \dot{V}_{out} ([O_2]_{in} - [O_2]_{out}) \right) \quad (\text{Eqn. 12})$$

where E is an empirically derived heat of combustion of oxygen taken as 13.1 ± 0.6 kJ/g, \dot{V}_{out} is the instantaneous flow rate out measured by the flow meter, $[O_2]_{in}$ is the oxygen concentration without combustion, and $[O_2]_{out}$ is the instantaneous oxygen concentration as measured by the oxygen sensor of the MFC. Finally, the Δh_c is found by integrating the instantaneous heat release rate over the duration of the test to get the total heat release in [kJ] and dividing by the initial mass of the sample. For more details on how the heat of combustion for solids is found, and why method B is used, refer to Raffan (Raffan-Montoya, Ding, & Stoliarov).

Because the mass flow rate of the solid samples is not explicitly known, a theoretical estimation of the mass flow rate is found using HRR and heat of combustion of the tests. The mean heat release rate can be found by averaging the instantaneous heat release rate values found from Eqn. 12 over the period of image acquisition (which

corresponds to the steady period of the flame's development). This mean heat release rate in units of [kW] is then divided by the computed Δh_c to get a mean mass loss rate during the acquisition period, in units of [g/s]. With a mass loss rate known, the true heat release rate that corresponds to the conditions of the MFC can be found by multiplying by the measured Δh_c , or the total heat release rate can be found by multiplying by the complete heat of combustion (calculated from the heats of formation).

2.5 Calculation of flame-to-gauge heat transfer

With the radius and intensity profile functions determined and the corrected heat flux gauge data sorted, all contributions from the images are completed and geometric calculations of the flame interaction with the heat flux gauge can then be calculated. Using the measured total heat release rates and the parameters found from the radiation measurements, the spatially-resolved radiation fraction and the radiative fraction can be found.

2.5.1 Establishing geometric considerations

In order to calculate radiation exchange between the flame and the heat flux gauge, geometric definitions must first be established. Because the radiation exchange is calculated numerically using a MATLAB script, the geometric parameters must be presented in symbolic form in order to be manipulated. Such parameters include the resolution and position of differential elements of the flame surface, the normal vectors of the flame sheet and the gauge face, and the vector that connects a differential element to the gauge face. These parameters are discussed here.

As previously mentioned, the origin of the Cartesian coordinate system is placed at the geometric center of the top of the burner. The z -axis extends from the origin in the vertical direction (parallel to the flame axis), the x -axis runs parallel to the camera lens and the y -axis runs parallel to the heat flux gauge. The location of the heat flux gauge is defined by the center of the detection surface at the coordinates (x_g, y_g, z_g) and the heat flux gauge lies in the y - z plane and runs parallel to the y -axis (as shown in Figure 11). The unit vector normal to the face of the gauge surface is given as $\vec{n}_g(x_g, y_g, z_g)$. The heat flux gauge is assumed to have an infinitesimally small detection surface.

The radius profile determined in Section 2.3.3 is used to construct a theoretical 3-dimensional, axisymmetric flame. The reconstructed 3-D flame is shown in Figure 11. Due to an assumption of symmetry about the burner axis, the radius of the flame is constant for any height along the flame. The 3-dimensional flame is constructed by first scanning by small vertical increments dz , which is taken as one pixel-length

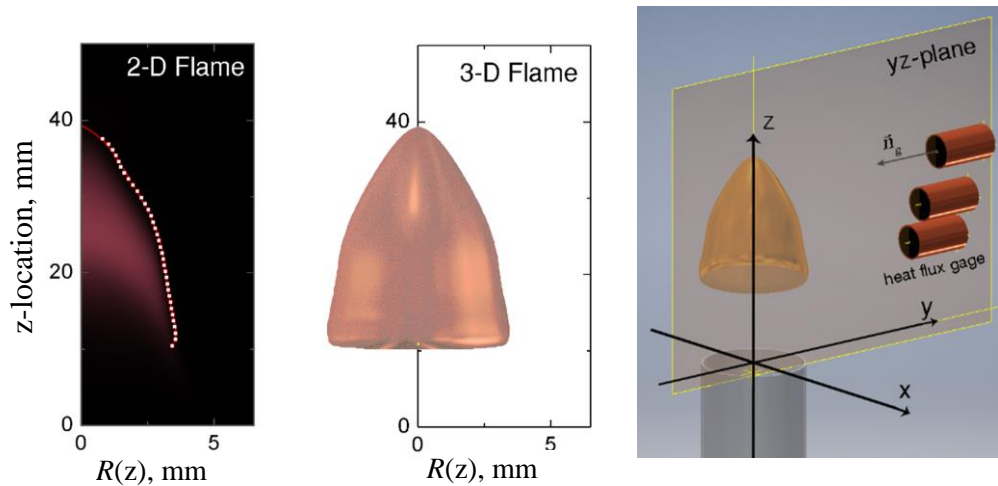


Figure 11. 2-D and 3-D rendering of the axisymmetric flame. Images are not to scale.

(~0.016mm), and then sweeping in the radial direction in small angle $d\theta$. The vertical distance from the origin is defined as some length h . The sweeping angle θ is defined with respect to the y-axis and starts at $\theta = 0$. The differential angle $d\theta$ is a function of $R(h)$ and is changes with z-location in order to ensure that the arc length is nearly constant amongst all differential elements on the flame sheet (this results in nearly constant differential areas of elements and therefore avoids unintentional favoring of a particular region of the flame). With each sweep of length dz and angle $d\theta$, a small differential element of the flame is created and this element has an area $dA_p(h, \theta)$. The differential area of each element is computed as:

$$dA_p(h, \theta) = R(h)d\theta \sqrt{\left(\frac{\delta R(h)}{\delta z} dz\right)^2 + (dz)^2} \quad (\text{Eqn. 13})$$

where $\frac{\delta R}{\delta z}$ is the local derivative of the radius profile $R(z)$ with respect to the z-direction.

The differential element location is also needed for finding the radiation exchange between the flame and the gauge. The position of each surface element is defined by a Cartesian location (x_p, y_p, z_p) and is related to the radial location $(R(h), \theta)$ by:

$$x_p = R(h) \cos \theta; \quad y_p = R(h) \sin \theta; \quad z_p = h \quad (\text{Eqn. 14})$$

Within this definition, the position of any radiating element can be defined by a height h and a radial angle location θ , which takes on a value between 0 and 2π . With the system in place for defining the position of radiating elements of the flame and knowing that the flame sheet is a series of differential elements, the Cartesian equation of the flame sheet surface, F , is given by:

$$F(x_p, y_p, z_p) = x_p^2 + y_p^2 - R^2(z_p) = 0 \quad (\text{Eqn. 15})$$

This function $F(x_p, y_p, z_p)$ describes the flame sheet that is shown in Figure 11

Another important geometric parameter is the vector normal to each flame element, $\vec{n}_p(x_p, y_p, z_p)$. This vector is needed in order to compute the interaction between the individual element and the face of the gauge. Because a symbolic function for the flame sheet is given by $F(x_p, y_p, z_p)$, mathematic operations can be used to find the normal vector at any particular point on the flame sheet. The flame sheet function $F(x_p, y_p, z_p)$ is particularly desirable because it is a differentiable scalar function that is equal to a constant value, $F(x_p, y_p, z_p) = 0$, as shown by Eqn. 15. In the special case that a function describing a surface is differentiable and equal to a constant, and that the gradient of the function at a point on the surface is not the zero vector, then the gradient of the function is the normal vector of the surface (Kreyszig). The surface function of the flame $F(x_p, y_p, z_p)$ meets the criterion to apply this theorem, and therefore the normal vector at any point (x_p, y_p, z_p) can be found by taking the gradient of the surface function. In equation form, the normal vector to each flame element is found by:

$$\vec{v}_p(x_p, y_p, z_p) = \nabla F(x_p, y_p, z_p) = \nabla[x_p^2 + y_p^2 - R^2(z_p)] \quad (\text{Eqn. 16})$$

Obtaining the unit normal vector is desirable, so therefore the vector is normalized by the vector's magnitude and the unit normal vector is found as:

$$\vec{n}_p(x_p, y_p, z_p) = \frac{\vec{v}_p}{\|\vec{v}_p\|} \quad (\text{Eqn. 17})$$

The gradient of the surface function can be performed symbolically and then simply solved numerically by plugging in the Cartesian coordinates of any element on the

flame sheet. This approach provides a clean and computationally lean method for finding the unit normal vector.

The final geometric parameter to calculate is the unit vector that points from the differential element and the center of the gauge face. Because the locations of these two points are known, the vector connecting them is simple to find. The vector connecting a point on the flame surface and the gauge is taken to be:

$$\vec{v}_{pg}(x_p, y_p, z_p) = (x_g - x_p)\hat{i} + (y_g - y_p)\hat{j} + (z_g - z_p)\hat{k} \quad (\text{Eqn. 18})$$

The geometry of \vec{v}_{pg} , \vec{n}_p and \vec{n}_g is shown in Figure 12. It is desirable to convert \vec{v}_{pg} into a unit vector, and this is done in a similar manner to Equation 17 by dividing \vec{v}_{pg} by its own magnitude, or:

$$\vec{n}_{pg}(x_p, y_p, z_p) = \frac{\vec{v}_{pg}}{\|\vec{v}_{pg}\|} \quad (\text{Eqn. 19})$$

The separation distance S between any point and the heat flux gauge is the magnitude of the vector \vec{v}_{pg} , or in equation form:

$$S = \|\vec{v}_{pg}\| \quad (\text{Eqn. 20})$$

All of the important geometric locations and vectors are known, allowing for the calculation of radiation properties.

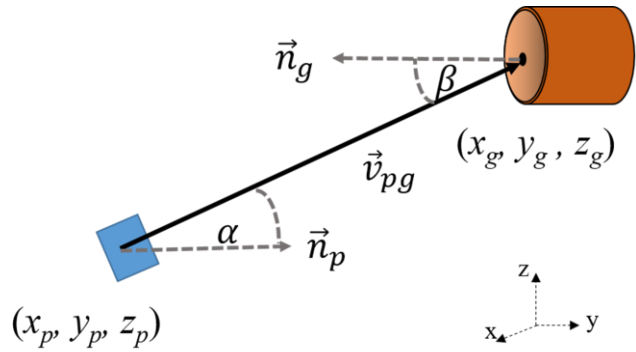


Figure 12. Geometry showing two differential objects in space.

2.5.2 Modeling the flame-gauge interaction and acquiring $c(z)$ and $I_f(z)$

The geometric considerations discussed in Section 2.5.1 are important for relating the radiation leaving the flame to the heat flux detected by the heat flux gauge. One objective of this study is to find a spatially-resolved radiation intensity profile [kW/m²-sr]. This radiation intensity profile is not equal to the centerline intensity $I_c(z)$, but this method provides a means of using the centerline intensity to find the radiation intensity of the flame $I_f(z)$. The assumption of axi-symmetry results in all emitting elements at a particular height h having the same radiation intensity, and therefore $I_f(z)$ is solely a function of z -location.

As mentioned, the radiation intensity is assumed to be proportional to the centerline intensity profile determined from the image processing methods, and the primary unknown is a relation function $c(z)$ [kJ/m²-sr] that is determined through inverse modeling of the heat flux gauge data and flame-gauge interaction. In equation form, the radiation intensity $I_f(z)$ is found by:

$$I_f(z) = I_c(z) * c(z) \quad (\text{Eqn. 21})$$

Therefore, in order to know the radiative intensity, the relation function $c(z)$ must be found first.

The expression that is used to find the relation function is the equation describing the heat flux from the flame to the gauge. The heat flux at the gauge is related to the radiation intensity $I_f(h)$ by the expression:

$$\begin{aligned} \dot{q}''_{gauge} &= \sum_{A_f} \frac{I_f(z) |\vec{n}_p \cdot \vec{n}_{pg}| (\vec{n}_g \cdot \vec{n}_{pg}) dA_p}{s^2} & \text{(Eqn. 22)} \\ &= \sum_h \sum_{\theta} \frac{I_c(h) c(h) |\vec{n}_p \cdot \vec{n}_{pg}| (\vec{n}_g \cdot \vec{n}_{pg}) R(h) d\theta \sqrt{\left(\frac{\delta R(h)}{\delta z} dz\right)^2 \delta + dz^2}}{(R(h) \cos \theta - x_g)^2 + (R(h) \sin \theta - y_g)^2 + (h - z_g)^2} \end{aligned}$$

There are important assumptions that are critical to Equation 22. First, the math contains an implicit assumption that the flame does not absorb any radiation. Secondly, the $|\vec{n}_p \cdot \vec{n}_{pg}|$ term of Equation 22 is in absolute value bars because the flame sheet is assumed to radiate in both directions from the flame sheet. By taking the absolute value of the dot product, the normal vector of the radiating element will always be facing in the direction of the heat flux gauge, therefore accounting for all radiation leaving the flame (from both sides of the flame sheet).

Equation 22 presents a direct relation between I_c and \dot{q}''_{gauge} and the only unknown is the relation function $c(h)$. For each flame height of a particular fuel, there are at least three heat flux gauge placements and three corresponding \dot{q}''_{gauge} values. In order to resolve $c(h)$ as a function of height, $c(h)$ is calibrated (or optimized) using Equation 22 at three heat flux gauge placements. This is done in an iterative fashion, where a function of $c(h)$ is assumed and the predicted heat flux gauge values (at the three specified heights) are compared to the measured \dot{q}''_{gauge} values. The coefficients of the relation function are iterated until the percent difference between the predicted and measured heat fluxes ($|\dot{q}''_{gauge} - \dot{q}''_{gauge,pred}|/\dot{q}''_{gauge}$) is minimized. In order to

validate the optimized $c(h)$ values, “spot-checks” are considered for each fuel. In these spot-checks, the heat flux is estimated at a gauge placed at a height that is *not* one of the three gauge locations used in the optimization of the relation function. This estimated heat flux value is compared with actual heat flux gauge measurements at the spot-check height. If the optimized relation function is able to predict heat fluxes at locations outside of the optimization parameterization, then the relation function is deemed acceptable.

Using this iterative process, an optimized function for $c(h)$ is found for every flame height for every fuel and can be used to estimate the heat flux measured at a gauge placed at any position. Additionally, the optimized $c(h)$ is plugged into Equation 22 to determine a spatially-resolved radiation intensity $I_f(z)$, which is one of the primary outcomes of this methodology.

2.5.3 Calculation of the total flame radiation and the radiative fraction

The final calculations of this methodology include finding the total radiation [W] of the flame and the corresponding radiative fraction. With the radiation intensity known, the total radiation from the flame sheet is found by integrating the product of $I_f(z)$ and $dA_p(z)$ over the surface of the flame and accounting for the flame sheet radiating in both directions. The expression for computing the radiation emitted by the flame is:

$$\begin{aligned}\dot{Q}_{rad} &= 2\pi \sum_h \sum_{\theta} I_f(h) dA_p = 2\pi \sum_h \sum_{\theta} c(h) I_c(h) R(h) d\theta \sqrt{\left(\frac{\delta R(h)}{\delta z} dz\right)^2 + (dz)^2} \\ &= 4\pi \sum_h c(h) I_c(h) R(h) \sqrt{\left(\frac{\delta R(h)}{\delta z} dz\right)^2 + (dz)^2}\end{aligned}\quad (\text{Eqn. 23})$$

The 2π term comes from the radiation from both sides of the flame sheet. As can be seen, by assuming axisymmetry, the $d\theta$ term can be pulled out of the equation and Equation 23 can be integrated over the z-direction only.

With the radiation heat flux known, the final calculation is finding the radiative fraction χ_r . The radiative fraction is the ratio of the radiation heat release and the total heat release, or:

$$\chi_r = \frac{\dot{Q}_{rad}}{\dot{Q}_{tot}} \quad (\text{Eqn. 24})$$

As discussed in Section 2.4, the total heat loss is known and is derived from either the measured heat of combustion values (as calculated from MFC measurements) or the complete heat of combustion values as calculated from the heats of formation.

2.5.4 Validation of methodology and MATLAB analysis script

The method of flame reconstruction and shape factor calculation are validated by constructing axisymmetric shapes such as a cone or sphere and comparing the calculated view factor to the analytical solutions for the view factor. The calculation for the view factor between a differential surface and a solid differs slightly from the equation used in this study due to the assumption that the solid radiates only from one side of the surface.

The equation for the view factor from a differential surface to another is given by:

$$F_{1-2} = \frac{1}{A_1} \int_{A_1} \left[\int_{A_2} \frac{\cos(\beta)\cos(\alpha)}{\pi S^2} dA_2 \right] dA_1 \quad (\text{Eqn. 25})$$

where the geometry is the same as given in Figure 12. The differential surface dA_1 is taken to be infinitesimally small, and dA_2 is a particular elementary surface of the solid.

The first geometry used for validation is a simple sphere centered at the origin, with a differential-surface along the z-axis. This configuration is well studied and the analytical solution for the view factor is accepted (Chung & Sumitra, Radiation shape factors from plane point sources) as:

$$F_{1-2} = \left(\frac{r}{h}\right)^2 \quad (\text{Eqn. 26})$$

where r is the radius of the sphere and h is the z-location of the detector. This solution is valid for $h > r$. The validation case involved a sphere with radius of $r = 30$ (arbitrary units) centered at the origin and a detector placed at $h = 60$ units, with a differential step size $dz = \pi/64$. The radius profile of the sphere, $R(z)$, is defined as $R(z) = (r^2 - z^2)^{0.5}$, where z is varied between $-r < z < r$. The 3-dimensional setup of this case is shown in Figure 13, and the analytical and calculated solutions for this geometry are shown in Table 5. This simplified case shows that the calculation of the view factor is working as expected and is accurately predicting the geometric interaction between a sphere and a differential element, with a percent difference between calculated and analytical solutions of 0.653%.

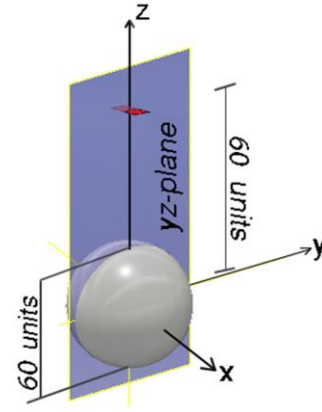


Figure 13. Spherical setup used in validation of view factor calculations. Image is not to scale.

Table 5. Analytical versus calculated view factor for validation configurations.

Geometry	Analytical Solution	Calculated Solution	% Difference (%)
Sphere	0.250	0.248	0.653
Cone	0.227	0.221	2.430

The second case involved a more complex geometry, which was an axisymmetric cone radiating to a differential element at any location (x,z) in the y-z

plane. This geometry is shown in Figure 14.

The cone is a normal cone ($r = l$) with radius of $r = 30$ units, height of $l = 30$ units and gauge placement of $(x,y,z) = (0, 35, 35)$. The radius profile of the cone is defined as $R(z) = l - z$, and a differential step size of $dz = 0.1$ units is used (a sensitivity analysis showed the solution

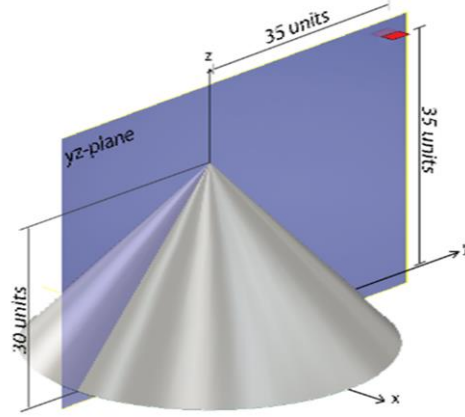


Figure 14. Conical setup used in validation of view factor calculations. Drawing not to scale.

was not dependent on the step size for any dz smaller than 0.1 units).

The analytical solution for the view factor from a cone to a differential element is given as (Chung, Kermani, & Naraghi):

$$\begin{aligned}
 F_{dA_1-c} = & \frac{\sin\beta}{\pi P} (S\sin\theta + P\cos\theta) \cdot \left[\tan^{-1} \left(\frac{H}{\cos\beta\sqrt{P^2 - S^2\tan^2\beta}} \right) - \tan^{-1} \left(\frac{S}{\cos\beta\sqrt{P^2 - S^2\tan^2\beta}} \right) \right] + \frac{1}{\pi} \left(\frac{H}{P} \sin\theta + \cos\theta \right) \\
 & \times \tan^{-1} \sqrt{\frac{P+S\tan\beta}{P-S\tan\beta}} + \frac{1}{\pi} \left\{ -\frac{H}{P} \sin\theta [(H-S)^2 \tan^2\beta + P^2 + H^2] + \cos\theta [(H-S)^2 \tan^2\beta - P^2 - H^2] \right\} \\
 & \times \frac{\tan^{-1} \sqrt{\frac{(H-S)^2 \tan\beta + P^2 + H^2 + 2P(H-S)\tan\beta}{(H-S)^2 \tan^2\beta + P^2 + H^2 - 2P(H-S)\tan\beta}} \cdot \frac{P+S\tan\beta}{P-S\tan\beta}}{\sqrt{[(H-S)^2 \tan^2\beta + P^2 + H^2]^2 - 4P^2 (H-S)^2 \tan^2\beta}} \quad (\text{Eqn. 27})
 \end{aligned}$$

where β is the half-angle of the cone ($\pi/4$ in this case), p is the y-location of the differential element, r_c is the radius of the base of the cone, s is the distance between the tip of the cone and the differential element, h is the z-location of the differential element, $P = p/r_c$, $S = s/r_c$, $H = h/r_c$, and θ is the angle between the normal vector of the differential element and the z-axis (in this case, $\theta = 0$). The values of the analytical and calculated view factors are shown in Table 5 and agreement between the two methods is within 2.5%, for various cone and gauge locations.

The agreement between the cone predictions and the analytical solutions show that the methodology and the code developed by the author is working as expected and captures the geometrical interactions of the setup. This validation test shows that the code can predict the radiation view factor between a solid body radiator and a differential element.

2.6 Sensitivity analysis of method

In order to properly understand the results presented in this section, this study includes an analysis of the radiative fraction's sensitivity to the various parameters of the method and the estimated uncertainty of the measurement. The sensitivity of the method is tested by shifting the user-defined parameters such that various elements of the methodology are altered, and quantifying the effect of this shift on the final measurement.

2.6.1 Choice of co-flow rate

The sensitivity of this method on the choice of co-flow rate is analyzed. In this analysis, identical experiments were carried out according to the experimental protocol with the exception of the air co-flow setting, which was set at either 1.81 SLPM or 3.0 SLPM. The study was carried out for two different gaseous fuels to study the effects on fuels with differing densities and viscosities. The first fuel studied was acetylene, a highly sooting flame with a high density. Methane was additionally studied due to its low density and unstable flames, presenting a flame that may be more prone to changing with a shift in air flow.

The results of this sensitivity analysis showed that the choice of co-flow, within the range studied, does not have an

Table 6. Radiative fraction for acetylene and methane at two differing co-flows of air.

	Acetylene	Methane
3.0 SLPM	0.261	0.069
1.8 SLPM	0.263	0.067
Std. Dev / Error	0.0012 / 0.00055	0.0017 / 0.0234

effect on the radiative fraction. For each co-flow choice, three trials are done and the mean radius and intensity profiles, in addition to the radiative fraction, are determined (the profiles are determined and averaged according to the procedure described in Section 2.3.3). The radiative fractions of the two co-flow settings for a 3.0cm propane flame are shown in Table 6, along with associated standard deviation and the standard error. As can be seen, the shift in co-flow has a larger impact on the radiative fraction of methane, with a 2.3% standard error between the two measurements. However, this error falls well within the uncertainty of the radiative fraction, which is found to be 10.0% (see Section 3.3.1). Therefore, it is determined that the choice of co-flow within a range of low co-flow rates (below 6 SLPM) makes negligible effects on the radiative fraction.

2.6.2 Choice of thresholding value

In order to understand the effect of this threshold choice on the radiative fraction, the entire methodology is applied in two cases that are identical (same images used, same heat flux gauge values, same processing code) with the exception of the threshold value specification. In one trial, the threshold value is set to the standard value of 7% of the maximum. In the other, the threshold value is made more lenient with a value of 3% of the maximum (see Figure 8 for visual representation of this difference). Each trial has its own distinct relation function to relate the flame characteristics to the

heat flux gauge readings. The results of this analysis showed that the radiation fraction is not sensitive to the threshold value. The difference in thresholding resulting in a 7.0% difference in surface area of the flame. However, the radiation fraction differed by less than 1.04% between the two resulting radiative fractions. This is likely because the areas that deviate most with a change in threshold value are the tip of the flame and the base of the flame. However, these regions of the flame fall in the lowest regions of the intensity curve, nearing zero at both the tip and the base. Therefore, because the radiative fraction results from a product of the intensity profile and the height-dependent surface area, the changes in radial profile have negligible effects on the final measurements of the radiation heat release rate and the radiative fraction.

2.6.3 Choice of bandpass filter

As mentioned in Section 2.1.2, a 900nm bandpass filter is placed on the lens of the camera. The effect of adding the filter was studied and compared to measurements without a filter on the camera, and the results showed that the relation function, $c(z)$, compensated for the addition of the filter. Due to the filter allowing a significantly lower amount of light into the lens of the camera, the exposure time setting of the camera must be changed to be much longer, in order to let in adequate light. Due to the change in exposure time (and the filter addition), the RAW intensity profile at the centerline changes accordingly. Because the intensity profile changes but the heat flux detected by the gauge is unchanged, the relation function is appropriately scaled by the change in intensity. Although the value of the intensity shifts with the addition of the filter, the shape of the intensity curve and z-location of the intensity peak stay unchanged. Therefore, there are no apparent spatial-spectral dependences that are

unaccounted for by the addition of the filter. The radiative fraction calculated from images with and without the filter on the camera differed by less than 1%, confirming that the relation function accounts for the addition of the filter.

2.6.4 Flame flickering

For some of the flames under consideration, dynamic instabilities caused slight “flickering” of the flame towards the tip of the flame. This occurred most notably in the highest flame height of the methane flame and the polyethylene flames. These fluctuations in flame result in radius profiles that have altered shapes, particularly near the top of the flame.

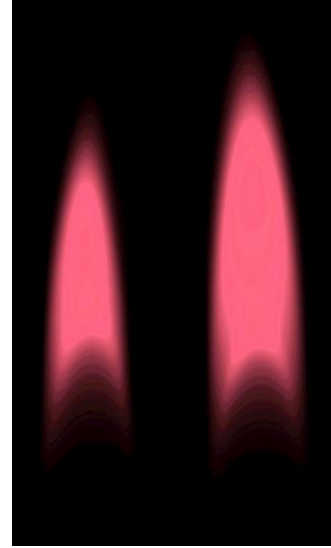


Figure 15. Two methane flames at low (left) and high (right) points of flame fluctuations. (NOTE: image color has been intensified for visual aid)

Visualization of this fluctuation is shown for methane flames in Figure 15. This flickering has the largest effect on the radius profile, which is based on the edge of the flame (as described in Section 2.3.3). And the radius profile has a significant effect on the radiative fraction due to its contribution to the relation function as well as the surface area of the flame sheet. The flickering is accounted for by the averaging scheme used in this methodology. Because 288 profiles are averaged together per flame height in order to obtain the mean flame radius (see Section 2.3.3 for radius profile determination and averaging scheme), the effect of flickering on the final radius profile is minimal; consequently, the effect of flame flickering on the radiative fraction is minimal.

2.6.5 Radius profile, centerline profile and heat flux gauge measurements

The final result of radiative fraction is not strongly sensitive to the radius profile fit to match the flame shape. A 12.0% change in radius profile location resulted in a change in radiation heat release rate and radiative fraction of only 1.5%. Therefore, a shift in radius profile contributes shyly to the uncertainty in the final measurement.

Next, the intensity profile is shifted to the within the uncertainty of the parameter, which is a 6%. This shift results in a 1.6% change in the radiation heat release rate and radiative fraction. Therefore, it is seen that the method is more sensitive to the intensity profile than it is to the radius profile (a smaller fractional error shift results in a larger change in radiative fraction). However, the contribution to the error of the radiative fraction is still relatively small.

The radiative fraction is perhaps most sensitive to the reading of the heat flux gauge. The radiative fraction has a proportional dependence on the heat flux reading (assuming that the heat flux gauge has a linear calibration). For example, a 10% deviation in the heat flux measured by the gauge will result in a 10% deviation in the radiative fraction. This high sensitivity is an additional reason why the convective contributions of the flame were carefully monitored with an extra-fine thermocouple in order to ensure no convective effects were included in the radiation calculations. Additionally, the water temperature of the water-cooled Schmidt-Boelter gauge was also monitored during all tests to ensure that there were no strong deviations from ambient temperature in the water line of the heat flux gauge. This is an important consideration since the heat fluxes of the flame are low and the heat flux at the gauge face based on measurements of temperature differences.

2.6.6 Mass flow rate and heat of combustion

Because the radiative fraction is proportional to the total heat release, the radiative fraction is also proportional to the mass flow rate and measured heat of combustion. Therefore, the method is sensitive to these parameters and leads to careful calculation and experimentation when finding the total heat release rate.

Chapter 3: Results

3.1 Results of radiation measurements

The radiation measurement experiments described in Sections 2.2, 2.3 and 2.5 lead to the determination of seven important parameters, namely $R(z)$, $I_c(z)$, h_f , \dot{q}''_{gage} , $c(z)$, $I_f(z)$ and \dot{Q}_{rad} . The results of these experiments are presented below.

3.1.1 Results of radius profile, $R(z)$

As discussed in Section 2.3, the radius profile results are the average profiles of 244 half-images (from nine trials, where each trial consists of 16 images). Each fuel flow rate is measured at three different heat flux gauge positions, and each heat flux gauge position is tested three times, hence the nine trials per fuel flow rate.

The resulting $R(z)$ profiles are shown in Figure 16. The solid lines indicate the 6th-order polynomial fit and the symbols represent the mean values of radius, found by following the description in Section 2.3. The uncertainty is taken as 2 standard deviations of this mean value and are shown; it should be noted that the uncertainty is on the order of the size of the marker, and is therefore not visible at all locations. The maximum uncertainty is 12.0% from the methane flame profile, and the mean uncertainty amongst all fuels and flame heights is less than 5.0%. The flame heights of each condition are also indicated with dashed lines.

Within the ranges of flames tested, acetylene and polyethylene tests surpassed the smoke point for at least one of the flame heights studied. The smoke point is observed visually with the “tails” at the tip of the flame and a chamber of smoke

escaping from the tip of the flame, as defined by Hurley et al. (Hurley, et al., 2016). All three of the acetylene flame heights were above the smoke point and the 4.5cm flame (15.5 °C/s heating rate) of the polyethylene also surpassed the smoke point.

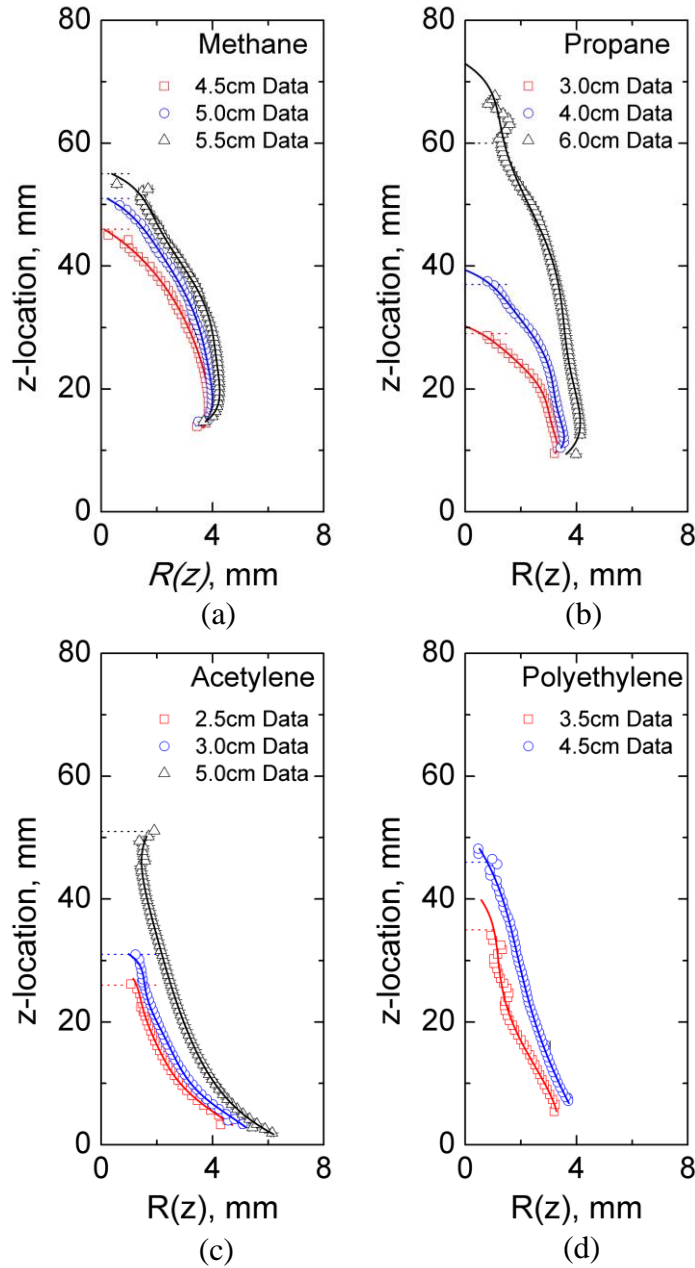


Figure 16. Radius profiles of (a) methane, (b) propane, (c) acetylene and (d) polyethylene flames. Mean flames heights (h_f) for each condition are indicated by dashed lines. The 6th-order polynomial fits for $R(z)$, as determined in MATLAB following the method detailed in Section 2.3.3, are shown with solid lines. Mean values with accompanying uncertainty is shown with symbols and error bars.

It is seen that the propane, methane and polyethylene flames are lifted approximately 10mm from the lip of the burner. This is consistent with the findings of Rankin et al., who acquired images of laminar ethylene diffusion flames from a circular burner of diameter 7.6mm with an infrared camera (Rankin, Blunck, & Katta). This is likely due to restrictions of measuring low-sooting regions of the flame within the range of 900nm, which would agree with the fact that methane (the lowest-sooting fuel) has the largest lift from the burner at around 13mm. Conversely, the acetylene flames differ from all of the other fuels by “anchoring” to the lip of the burner. The flame shape is also narrower and has inward curvature rather than the rounder flames of propane, methane and polyethylene. Additionally, because all acetylene flames are beyond the smoke point, the tip of the flame is not overtly clear due to a pillar of smoke escaping from the tip of the flame and the top of the radial profile not crossing the z-axis.

3.1.2 Results of centerline intensity, $I_c(z)$

The resulting profiles of the centerline intensity from the images, $I_c(z)$, are shown in Figure 17. Similar to the radius profiles, the $I_c(z)$ curves shown are the mean values of the 144 images taken from 9 trials per flame height. The mean values at each z-location are shown with symbols along with error bars that are given as 2 standard deviations of the mean. For all fuels and flame heights, the uncertainty is low with a maximum uncertainty of 5.8% at the tip of the 5.5cm methane flame and an average uncertainty less than 3% for all fuels. The accompanying trend lines represent the Gaussian fit discussed in Section 2.3.4. As can be seen, the acetylene flames have the highest $I_c(z)$ values due to the flame being highly-sooting and to all three flame heights being above the smoke point. Additionally, the acetylene profiles differ from the rest

of the fuels in shape, with a centerline intensity profile peaking at 10-30% of the flame height, rather than around 70% for the other fuels. This is related to the fact that the acetylene flames “anchor” to the burner lip, as discussed in Section 3.1.1. Additionally, the first-order Gaussian curvefit does not fully resolve the data; a sensitivity analysis was performed on this discrepancy by resolving the curve with a 6th-order polynomial

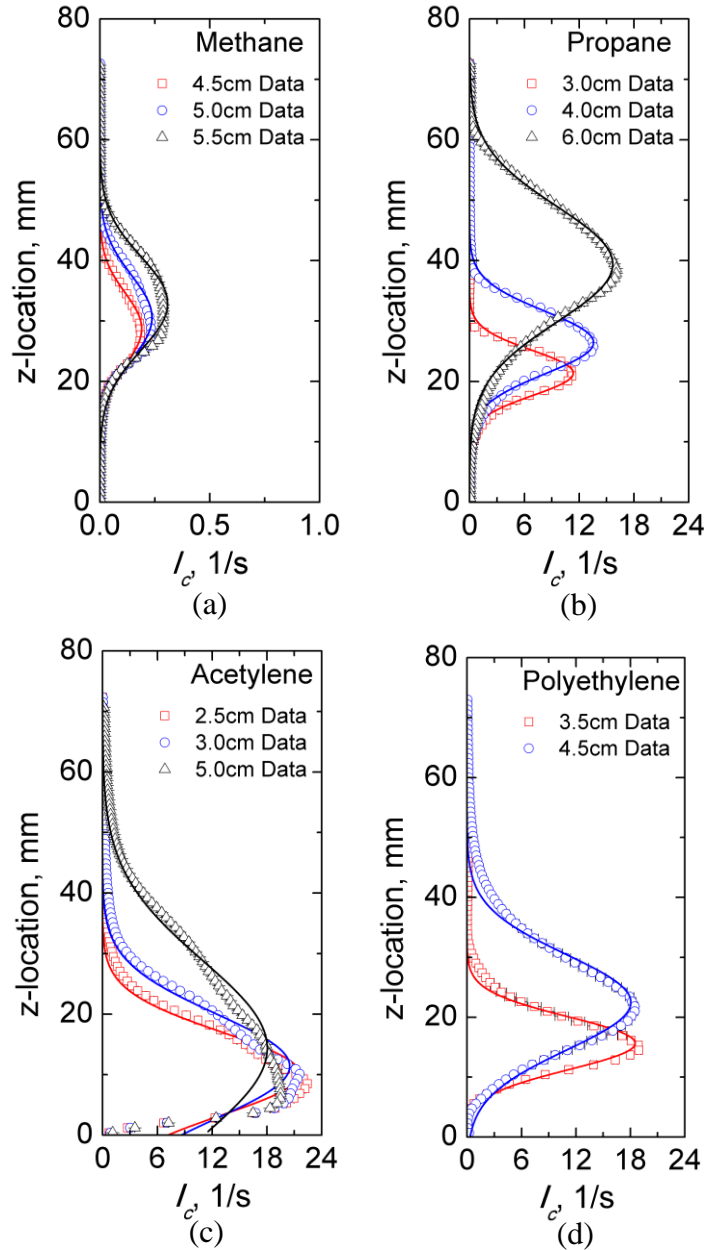


Figure 17. Centerline camera intensity profiles of (a) methane, (b) propane, (c) acetylene and (d) polyethylene flames. The mean Gaussian fits for $I_c(z)$, as determined in MATLAB following the method detailed in Section 2.3.4, are shown with solid lines.

and performing the methodology. This change in curve definition resulted in a 2.8% difference in the radiative fraction, which is within the uncertainty of the measurement. Therefore, the 1st-order Gaussian fit was used for all fuel types.

The polyethylene and propane flames have similar centerline intensity profiles to one another with maximum centerline intensities ~15-20 [1/s] and peak intensity locations at ~50-70% of the flame height. The low-radiation of the methane flame is evident with a peak I_c value being an order of magnitude lower than the rest of the fuels.

3.1.3 Results of flame heights, h_f

The flame heights of all tests are given in Table 7 and are shown graphically in Figure 16 (a)-(d). The values reported in the column “ h_f ” are the mean flame heights discussed in Section 2.3.3, and the rounded values in the column “Ref. Height” are the representative name that is used to reference each flame in the remaining sections of the results section. This reference flame name is used only to simplify notation. The uncertainty in the flame height measurements are on the same order of the uncertainty of the radius profile measurements. The mean uncertainty in the flame height is ~7% with a maximum uncertainty pertaining to the 3.5cm PE flame with an uncertainty of 17%.

As can be seen in Table 7, the flame heights fell within a range of 2.5 to 6.0cm, which is the range of flame heights desired within this study. As previously mentioned, most flames of solid fuels studied in the MFC have a flame height of around 2-6 cm for a range of heating rates between ~5-20 °C/s. As expected, the polyethylene flames fall within this range, with flame heights of 3.5cm and 4.6cm for heating rates of 8.0 °C/s and 15.5 °C/s, respectively.

Table 7. Results of h_f (and the accompanying reference name), gauge placement and mean \dot{q}''_{gage} for all experiments. Flames that exceed the smoke point are indicated with an asterisk (*).

Fuel	Conditions (sccm °C/s)	h_f (cm)	Ref. Height (cm)	z_g (cm)	\dot{q}''_{gage} (kW/m ²)
Propane	56.0	2.9	(3.0)	1.5	0.436
				2.5	0.368
				3.5	0.288
	69.6	3.7	(4.0)	1.5	0.578
				3.5	0.426
				4.9	0.297
	106.0	6.0	(6.0)	2.5	0.933
				3.5	0.833
				4.9	0.650
Methane	191.3	4.6	(4.5)	1.4	0.466
				2.4	0.425
				3.4	0.350
				4.9	0.264
	205.0	5.1	(5.0)	0.9	0.524
				1.4	0.491
				2.4	0.443
				3.4	0.384
				5.0	0.299
216.0	5.5	(5.5)	1.4	0.528	
			2.4	0.488	
			3.4	0.404	
			4.9	0.026	
Acetylene	94.8	2.6	(2.5)*	0.9	1.436
				1.4	1.287
				2.4	0.993
				4.9	0.462
	117.8	3.1	(3.0)*	0.9	1.842
				1.4	1.625
				2.4	1.266
	179.8	5.1	(5.0)*	4.9	0.642
				0.9	2.704
1.4				2.430	
2.4				2.411	
Polyethylene	8.0 °C/s	3.5	(3.5)	3.4	1.661
				4.9	1.135
				0.9	0.640
	15.5 °C/s	4.6	(4.5)*	1.4	0.357
				1.9	0.296
				1.5	0.883
				3.4	0.676
				5.0	0.447

It is worth noting that the range of flame heights for methane is smaller than the other fuels; this is due to thermo-physical restrictions of methane flames in this range of flame heights. Beyond a flow rate of 216.0sccm (corresponding to $h_f = 5.5\text{cm}$), the methane flame become unstable and bounced up and down on the burner, similar to a violent flickering. This condition makes it difficult for obtaining a steady flame and result in high amounts of scatter in both h_f and the $R(z)$. Therefore, the flames of methane are limited to a fuel flow rate of 216.0sccm. Additionally, there are limitations on flames with a fuel flow rate lower than 191.3sccm due to low radiative emission from the flames. Because methane in a low-carbon and therefore low-sooting flame, the radiation from methane flames is notably lower than the other gaseous and solid fuels studied. Therefore, methane flames shorter than 4.5cm result in heat flux measurements that near the noise of the heat flux gauge, which are not meaningful measurements. Therefore, the range of flame heights for methane are restricted to 4.5 to 5.5cm.

Additionally, it can be seen from Figure 16 that some of the recorded h_f values fall below the top of the mean radius data and the accompanying curvefit. This is a result of the method's definition of flame height, which is based on a mean value of the maximum height where a pixel has a greyscale value greater than 7% of the maximum greyscale value (as defined in Section 2.3.3). Because of variations in the height of the flame, the mean value of the maximum flame height falls below the data shown.

3.1.4 Results of heat flux gauge readings, \dot{q}''_{gauge}

The mean heat flux measured at the gauge face \dot{q}''_{gauge} is given in Table 7 for all fuels, flame heights and gauge heights. How the mean values are averaged and

obtained is described thoroughly in Section 2.3.1. The maximum corresponding uncertainty, taken as 2 standard deviations of the mean, was found to be 8.0%. This value is significantly larger than the intrinsic uncertainty of the gauge, which is given by the manufacturer as 3.0%. This discrepancy is likely attributed to an unsteady flame, rather than actual uncertainty in the gauge. In order to have a conservative estimate of the uncertainty in the radiative fraction, a fractional error of 8.0% is used to quantify the uncertainty.

It is seen that acetylene has the highest heat flux measurements, which agrees with the $I_c(z)$ findings. It is also seen that the maximum heat fluxes are measured closer to the base of the flame. This is attributed to the gauge being placed radially closer to the burner outlet as z_g approaches $z = 0$ (see Table 1 for gauge placements). All the gauge is translated up the height of the flame, the gauge must be moved away from the flame in the radial direction in order to avoid convective effects (as monitored by the thermocouple at the gauge). Therefore, as the gauge is pulled away from the centerline of the flame, the radiation drops off considerably, and the heat flux measured drops.

3.1.5 Results of relation function, $c(z)$

The relation function is calculated for all conditions using the inverse modeling approach explained in Section 2.5.2. The criterion for determining an adequate relation function is how well it is able to predict the heat flux measurements at a given gauge position. Table 8 shows the coefficients and curve specifications of the relation functions for all flames. The relation functions of flames that were below the smoke point were best represented by a 2nd-order polynomial curve and have the form $c = az^2 + bz + d$, whereas the flames above the smoke point were best represented by a linear curve with a shallow positive slope and have an equation of the form $c = az + b$. The relation functions of all flames are shown in Figure 18, which are split into two figures for clarity.

Table 8. Coefficients and curve specifications for the relation functions of all flames.

Fuel	Ref. Flame Height (cm)	Curve Type	a	b	d
Propane	(3.0)	Polynomial	3.57E-04	-1.54E-02	8.48E-01
	(4.0)	Polynomial	2.18E-04	-1.14E-02	6.83E-01
	(6.0)	Polynomial	2.13E-04	-1.70E-02	7.58E-01
Methane	(4.5)	Polynomial	1.38E-02	-7.86E-01	3.37E+01
	(5.0)	Polynomial	1.02E-02	-5.79E-01	2.43E+01
	(5.5)	Polynomial	6.57E-03	-4.49E-01	1.88E+01
Acetylene	(2.5)*	Linear	8.13E-03	5.05E-01	-
	(3.0)*	Linear	6.50E-03	5.23E-01	-
	(5.0)*	Linear	7.50E-03	4.88E-01	-
Polyethylene	(3.5)	Polynomial	5.01E-03	-1.31E-01	1.13E+00
	(4.5)*	Linear	1.92E-02	1.00E-01	-

These characterizations of 2nd and 1st order polynomial fits agree with the centerline intensity curves shown in Section 3.1.2; a higher c value corresponds to areas of the curve where the intensity is low, following the relationship $\dot{q}_{gauge} \propto c * I_c$. Conversely, locations of high centerline intensity have corresponding low c values. When looking at the relation functions in Figure 18, the z -location of the minimum value corresponds roughly to the peak of the $I_c(z)$ curves.

It should be noted that all of the relation functions have very shallow curves within the region of the flame. This is as expected because the relation function is in place to relate the spatially-resolved centerline intensities (as measured by the camera at a wavelength of 900nm) to the heat flux gauge measurements. This method assumes that the majority of the emission from the flame is captured by the camera due to the soot in the flame emitting strongly in the IR range. Therefore, following the assumption that the flame radiates primarily in the

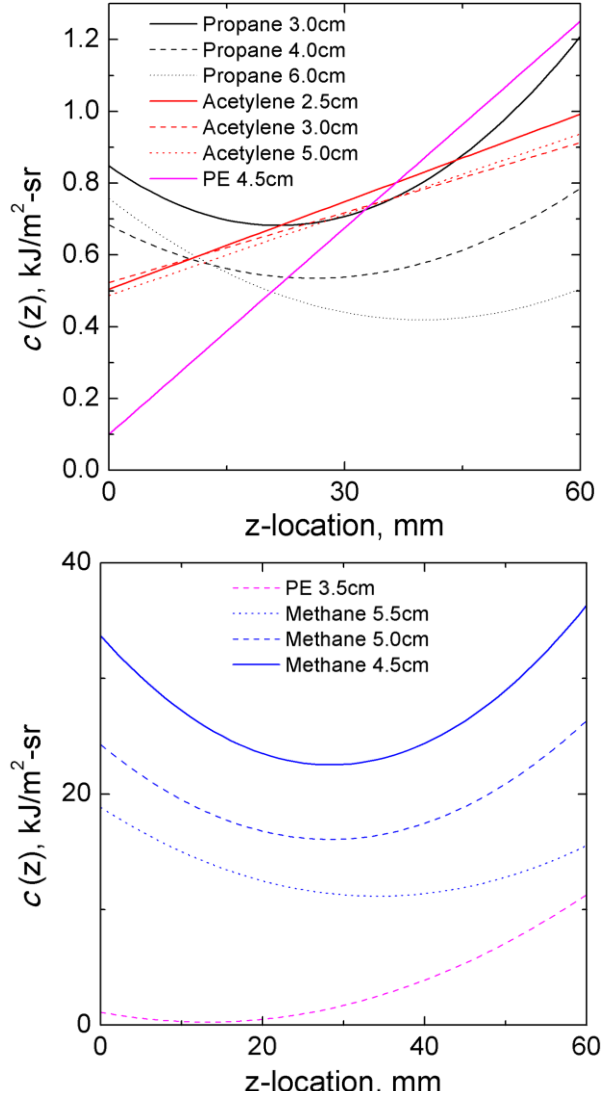


Figure 18. Relation function $c(z)$ curves for all fuels and flame heights. Figure broken into two figures for clarity across orders of magnitude.

region around 900nm, the relation function should not vary greatly along the height of the flame. The exception to this is methane, which emits in lower regions of the spectrum due to lower soot production (as discussed in Section 3.1.2). As can be seen, the relation function takes on much larger values for methane (due to low centerline intensity) and has a stronger dependence on the z-location in the flame. This is because the regions near the burner outlet ($z = 0\text{mm}$) and near the tip of the flame are low-

emission regions. The relation function is in place to compensate for the emission that is not captured by the camera, and therefore has a higher value for these low-emission regions.

The inverse-modelled relation functions are able to predict the heat flux at the gauge face with a mean relative difference of 7.2% (for all fuels, flame heights, and gauge positions), with a maximum deviation of 20% at the lowest gauge location of the short polyethylene flame. The relation function showed to be a valuable predictor of heat fluxes outside of the flame region as well, predicting the heat flux within 20% for gauge heights up to 1.2 times the flame height. Figure 19 shows the representative predictions versus measured \dot{q}_{gauge} values for one flame height for each fuel (all flame heights are not shown in order to avoid over-crowding of the figure). The measured

(open symbols with uncertainty) and predicted (closed symbols) \dot{q}_{gauge} values are plotted against a normalized flame height axis, which allows for a better understanding of how the relation function predicts heat flux within the flame

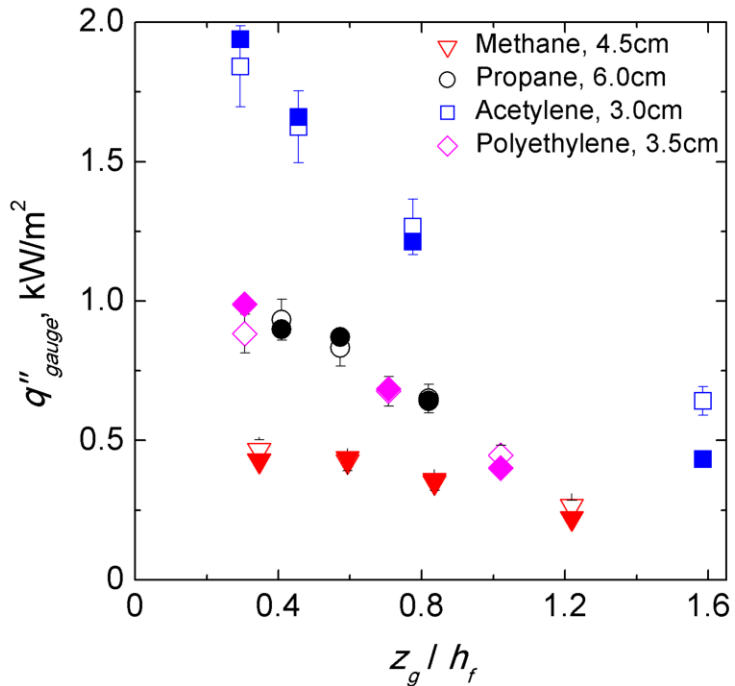


Figure 19. Measured (open symbols) values of \dot{q}_{gauge} versus predicted \dot{q}_{gauge} values (filled symbols) using the relation functions shown in Figure 17.

region (within high-radiation regions). As can be seen for all fuels, the relation function is able to predict the heat flux gauge readings within the uncertainty of the heat flux gauge measurements within the flame region ($z_g/h_f < 1$). Even beyond the flame region, the relation function does an adequate job of predicting the heat flux, as can be seen in the methane curve at $z_g/h_f = 1.25$.

3.1.6 Results of flame radiation intensity, $I_f(z)$

The flame radiation intensity $I_f(z)$ [kW/m²-sr] is found by multiplying the centerline intensity profiles from Section 3.1.2 by the spatially-resolved relation functions of Section 3.1.5. The resulting curves are shown in Figure 20. The resulting functions are representative of the radiation profile along the height of the flame and represent the intensity with which all elements at a given z-location emit (per unit area and steradian). The results for $I_f(z)$ are consistent with the findings for $I_c(z)$ and $c(z)$, with acetylene having the highest radiative intensity and methane having the lowest, with propane and polyethylene giving very similar $I_f(z)$ curves. For the propane, methane, and acetylene flames, the peak $I_f(z)$ values are fairly consistent amongst all flame heights. The exception to this is polyethylene, which has a much higher peak radiation intensity value for the higher flame height, as seen in Figure 20(d). This is likely due to the lower flame height being below the smoke point and the higher flame height being above the smoke point.

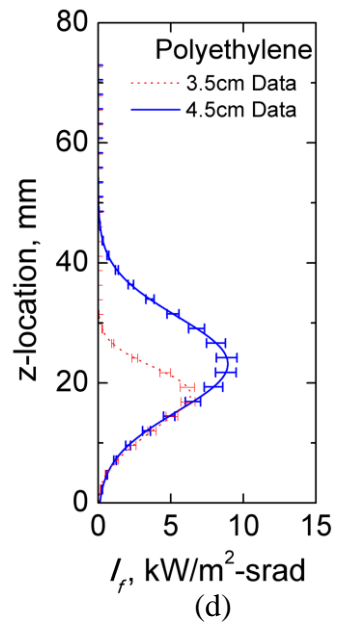
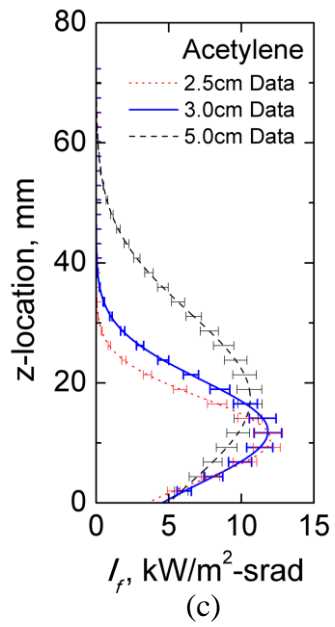
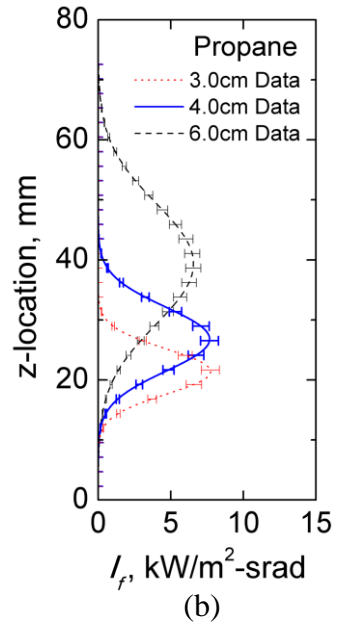
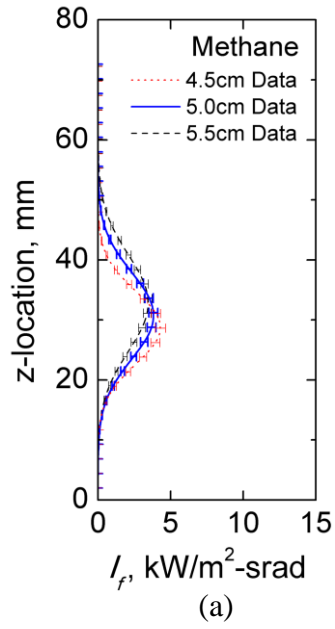


Figure 20. Radiation intensity profiles of (a) methane, (b) propane, (c) acetylene and (d) polyethylene flames.

3.1.7 Results of total radiation, \dot{Q}_{rad} .

With the radiation intensity and the shape of the flame known, the total flame radiation \dot{Q}_{rad} [kW] can be found using Eqn. 23 from Section 2.5.3. The resulting flame radiation values along with their uncertainty are shown in Figure 21.

Once again, acetylene has the highest radiation heat release rate, ranging between 20 and 45 kW over a range of flame heights. Methane has the lowest radiation heat release, with values below 10 kW for all flame heights. Propane and polyethylene gave similar radiation, ranging between 6 and 20 kW for a wide range

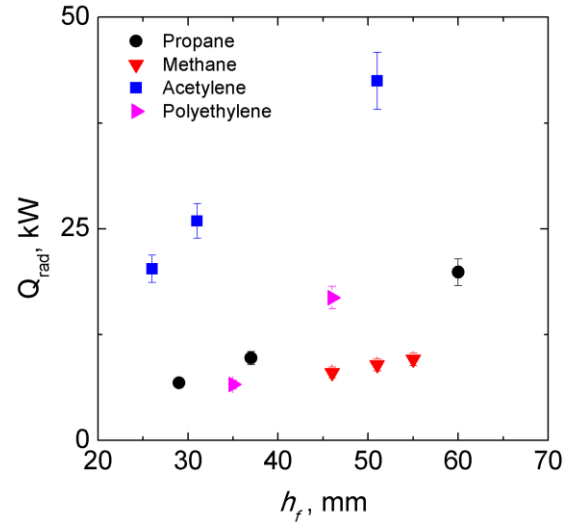


Figure 21. Total radiation \dot{Q}_{rad} [kW] of flames plotted against the measured flame heights.

Table 9. Total radiation \dot{Q}_{rad} [kW] of all flames.

Fuel	Flame Height (cm)	Q_{rad} (W)
Propane	3.0	6.8
	4.0	9.7
	6.0	19.9
Methane	4.5	8.0
	5.0	8.9
	5.5	9.6
Acetylene	2.5	20.3
	3.0	25.9
	5.0	42.5
Polyethylene	3.5	6.6
	4.5	16.9

of flame heights. The numeric values for \dot{Q}_{rad} for all flames are given in Table 9.

The uncertainty in the value of \dot{Q}_{rad} is dominated by the uncertainty of the heat flux gauge, \dot{q}''_{gage} , which has an uncertainty of 8.0%. Therefore, the uncertainty in the total radiation is estimated to be 8.0%.

3.2 Results of heat of combustion experiments

The results of the heat of combustion tests done in the MFC are compiled and compared to the calculated total Δh_c and literature values in Table 10. The mean values measured in the MFC according to the method described in Section 2.4 are in bold typeface and the accompanying standard error in the measurements are shown. The total Δh_c calculated using the heats of formations and a stoichiometric combustion reaction approximation are also shown. Due to a lack of literature data on the heat of formation of volatilized polyethylene, the total Δh_c is taken as the heat of combustion obtained from oxygen bomb calorimetry by Tewarson (Tewarson, 2008). This value accounts for energy lost to incomplete combustion and char, so is comparable but not precisely equivalent to the total Δh_c values obtained from the heats of formation.

Table 10. Measured heat of combustion values for all fuels. Measured values are compared to complete heat of combustion values either calculated from the heats of formation or taken from literature values from oxygen bomb calorimetry.

Fuel	Flame Height (cm)	Mean Δh_c [J/kg]	Std. Error (+/-) [J/kg]	Complete Δh_c (from ΔH_f or Oxy. Bomb), [J/kg]
Methane	5.0	51	0.3	50
Propane	3.0	46	0.4	46
	4.0	47	0.3	
Acetylene	2.5	35	0.1	48
Polyethylene	3.5	44	0.4	44 [Tewarson]

The tests for methane, acetylene, and polyethylene are done at the middle flame height to obtain a heat of combustion that is assumed to be applicable to any flame of that fuel within the scope of this study. This assumption is checked by measuring the heat of combustion of propane at two separate flame heights. These values fall nearly within the scatter of one another, and therefore this assumption is deemed acceptable.

In all cases except the acetylene tests (which is highly sooting and therefore far from complete combustion), we expect the measured heat of combustion to be close to the maximum oxygen consumption value. As can be seen in Table 10, propane and methane's measured heat of combustion values fall within 2.5% of the theoretical oxygen consumption value. For acetylene, due to considerable heat losses to soot production, the measured Δh_c values are roughly 25% lower than the total Δh_c calculated. Therefore, the measured heat of combustion values are used in the further analysis of the radiative fraction. Additionally, the measured polyethylene heat of combustion fell within the range of literature values provided by Tewarson (Tewarson, 2008) and Quintiere (Quintiere, Lyon, & Crowley), and will therefore be used moving forward.

The uncertainty in the measurements of the heat of combustion is 5.0%, according to Raffan (Raffan-Montoya, Ding, & Stoliarov). This error comes primarily from uncertainties in the mass flow meter signal, but also has contributions from uncertainties in measured mass and species concentrations.

3.3 Results of total heat release rate and radiative fraction

3.3.1 Results of total heat release, \dot{Q}_{tot}

With the heats of combustion (both measured and complete) known, the total heat release can be found for all tests using the mass loss rate. For gaseous fuels, the mass loss rate is known directly from the digital flow controllers of the MFC apparatus. For the solid fuels, the mass flow rate is determined over the period of image acquisition

by using the instantaneous heat release rate [kW] and the measured heat of combustion.

Detailed description of obtaining \dot{m} for solid fuels is given in Section 2.4.2.

Table 11. Compiled heats of combustion, total radiation loss, and radiative fraction for all fuels and flame heights.

	Propane			Methane			Acetylene			Polyethylene	
Flame Height [cm]	3.0	4.0	6.0	4.5	5.0	5.5	2.5	3.0	5.0	3.5	4.5
$\Delta h_{c,eff}$ [J/kg]	46	47	-	-	51	-	35	-	-	44	-
$\Delta h_{c,com}$ [J/kg]	46	46	46	50	50	50	48	48	48	44	44
Q_{tot} [W] (effective)	78.9	98.1	149.3	106.4	114.2	120.4	59.7	74.2	113.2	36.3	49.0
Q_{tot} [W] (complete)	78.6	97.7	148.8	103.8	111.4	117.4	67.7	84.1	128.3	39.1	52.8
χ_r (effective)	8.9	10.2	13.7	7.8	8.1	8.2	35.0	36.0	38.7	18.8	35.5
χ_r (complete)	8.9	10.3	13.8	8.0	8.3	8.4	30.9	31.8	34.1	17.4	32.9

The measured and complete values of \dot{Q}_{tot} are given in the second row of Table 11 for all flame heights. The corresponding heats of combustion and radiative fractions are also included in Table 11. The range of total heat release varied from 40 to 150 kW across all fuels. The uncertainty in the values of \dot{Q}_{tot} is on the order of the uncertainty of the heat of combustion measurements, which is 5% (Raffan-Montoya, Ding, & Stoliarov). It is worth noting that the \dot{Q}_{tot} values for the polyethylene are significantly lower than the gaseous fuels for similar flame heights. This is not due to lower heats of combustion, but rather due to the addition of 50sccm of the purge gas N₂. This purge gas is needed to carry the volatiles of the solid fuel sample out of the burner tube, so similar flame heights are obtained but the mass flow rate of actual volatiles is diluted and much lower than that of the gaseous fuels. In comparing mass flow rates, the calculated mass flow rate of the 4.5cm polyethylene flame is an order of magnitude lower than that of the 4.5cm methane flame. This is where the discrepancy in total heat release rate originates.

3.3.1 Results of radiative fraction, χ_r

Table 11 also shows the final results for the radiative fraction, χ_r , which are found by Eqn. 24, $\chi_r = \dot{Q}_{rad}/\dot{Q}_{tot}$. Due to the two definitions of \dot{Q}_{tot} , there are two corresponding radiative fractions reported (measured/complete). The results show that for each fuel, an increase in flame height (or synonymously an increase in total heat release rate) results in an increased radiative fraction, a finding consistent with those of Markstein (Markstein G. , 1984).

The uncertainty in the value of χ_r can be found by propagating the uncertainty of the various parameters that are integrated into the calculation of the radiant fraction. The primary contributors to the uncertainty in the radiative fraction are the heat flux gauge readings and the heat of combustion used. A simplified estimate of the uncertainty of the radiative fraction can then be found based on the fractional uncertainties of \dot{q}''_{gage} and Δh_c . This is found by taking the square root of the sum of the squares of the fractional error, or in equation form, $\frac{\delta\chi_r}{\chi_r} =$

$$\sqrt{\left(\frac{\delta\dot{q}''_{gage}}{\dot{q}''_{gage}}\right)^2 + \left(\frac{\delta\Delta h_c}{\Delta h_c}\right)^2} \text{ where } \frac{\delta\chi_r}{\chi_r} \text{ is the fractional uncertainty in the radiative fraction.}$$

This analysis shows that the estimated uncertainty is on the order of 10.0% of the calculated radiative fraction.

Of the gaseous fuels, acetylene has the highest radiative fraction, which agrees with literature values that state acetylene having radiative fractions significantly higher than other gaseous fuels (Markstein G. , 1984). Additionally, as is seen in the polyethylene tests, a transition above smoke point results in a noticeable increase in the radiative fraction.

3.4 Comparison to literature values

To best understand how these results compare to previous studies, the values of total heat release rate and radiative fraction must be altered to match the assumptions of the literature. Considering Markstein's work is the literature's most thorough study of laminar flame radiation, the results will be altered to match the assumptions of (Markstein G. , 1984). In Markstein's study, a theoretical (complete) Δh_c is used to define the total heat release rate. Therefore, the values for total heat release is taken from the complete Δh_c column from Table 11 in the place of the measured Δh_c . The corresponding value of χ_r is consequently used in the comparison as well, and these values are compared to literature data.

3.4.1 Propane and methane flame comparison

The radiative fraction data for fuels that did not reach smoke point at any flame height, which include propane and methane, are shown in Figure 22. The data of Markstein (Markstein G. , 1984) and Escudero (Escudero & al.) is also shown for a comparison to previous studies. It is worth mentioning that the data of Markstein has not been altered, but the data of Escudero has been corrected from a definition of chemical heat of combustion to that of a "complete" heat of combustion, and the data of the current study is taken as the "complete" Δh_c and the corresponding radiative fraction. These corrections are done by multiplying the total heat release rate by the complete Δh_c and dividing by the chemical $\Delta h_{c,chem}$. On the other hand, the values of χ_r are multiplied by the chemical $\Delta h_{c,chem}$ and divided by the complete Δh_c .

The measured values from the current study for propane fall roughly 25% below the data of Markstein, and the data of Escudero falls between Markstein's data and the current study's data. This could be attributed to many differences in methods, including geometric considerations, differences in apparatus or assumptions made.

A noticeable difference in the method used by Markstein and the present study is the location of the radiometer. In order to test the

method's sensitivity to gauge placement and provide a

meaningful comparison to Markstein's data, Markstein's method is replicated. The spherical isotropy assumption is made in line with Markstein; hence, this replication is called the "4 π -Method" because of the 4 π term in the mathematical expression of spherical isotropy. The gauge placement of Markstein's data was given as 30 cm, so the gauge location of the prediction is specified at 30 cm from the flame axis and at a height of half of the flame height. Using the radius and intensity profiles, as well as the

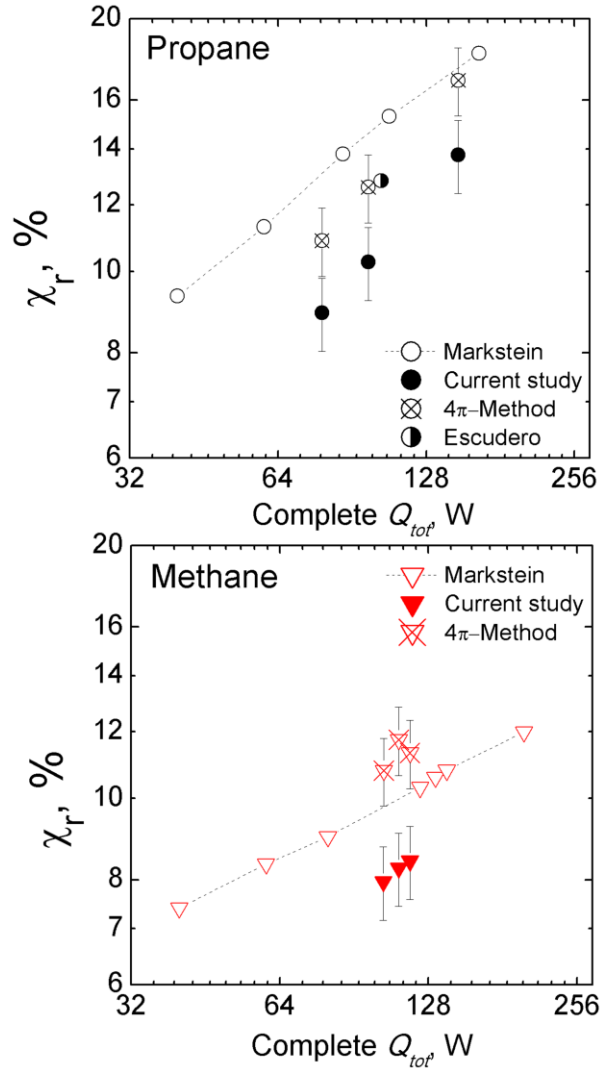


Figure 22. Measured radiative fractions for methane and propane, in addition to literature values. The figure is plotted on a log2-log2 axis.

relation function $c(z)$, the heat flux detected by the gauge (as would have been seen in Markstein's experiments) can be predicted at any location. With the heat flux to the gauge known, an assumption of spherically isotropic emission is made in accordance with Markstein, and the radiative portion of heat release is calculated as:

$$\dot{Q}_{rad} = 4\pi S_y^2 \dot{q}''_{gage} \quad (\text{Eqn. 28})$$

where S_y is the distance from the gauge to the flame axis and \dot{q}''_{gage} is the estimated gauge heat flux reading. This reconstructed scenario, with the flame treated as a point source, provides a more meaningful comparison between the measured flames and the data of Markstein and highlights potential erroneous assumptions in previous studies where spherical isotropy is assumed.

By predicting measurements at a gauge location of $x_g = 30$ cm and using the spherically isotropic emitter assumption, the radiative fractions of propane fall within the uncertainty of Markstein, indicating that geometric factors influence the measurement of radiative fraction. Escudero studied laminar flames in the "nearer" field at a distance of 120mm with a Schmidt-Boelter gauge by sweeping the gauge along the height of the flame. Radiation heat flux is then estimated by assuming cylindrical isotropy and the heat flux readings are then integrated over the height of the flame to obtain the radiative heat release rate. The radiative fraction measured by Escudero falls below Markstein's data and in line with the 4π -method data.

The measured values of radiative fraction for methane fall about 20% below those of Markstein. With the spherically isotropic emission consideration, the values for methane jump above those of Markstein, but fall within the error of the measurements. Due to methane being a low-intensity emitting flame, resolving the

intensity along the height of the flame may be important in the calculations of the radiative heat loss, as indicated by a significant jump in radiative fraction when a spherically isotropic assumption is made.

3.4.2 Acetylene and polyethylene flame comparison

The measured values for fuels that were able to exceed the smoke point for at least one flame height, namely acetylene and polyethylene, are shown in Figure 23. Markstein did not present data for acetylene or polyethylene, but the data region for low-smoke-point fuels are shown, which include the alkene and butadiene fuels. This data region is broken into the radiative fraction before and after the smoke point was reached, as shown by the differential shading of the region. Markstein noted that acetylene values in his study were noticeable higher than the other fuels and were not included due to potential differences in the assumption of optical thickness (Markstein G. , 1984). As seen in Figure 23, the measured acetylene values fall along the region of highly sooting flames, and the values altered with the 4π -method jump above the values of this region, as expected. The values are not as high as 50%, which were reported as a maximum value by Sivathanu (Sivathanu & Gore, 1994), who studied radiation of laminar acetylene/air flames in a similar configuration to Markstein (Markstein & De Ris, 1985). However, the mean radiative fraction of an acetylene flame found by Sivathanu was around 45-46%, as indicated in Figure 23. This value agrees well with the trend shown by Markstein and the present study's data.

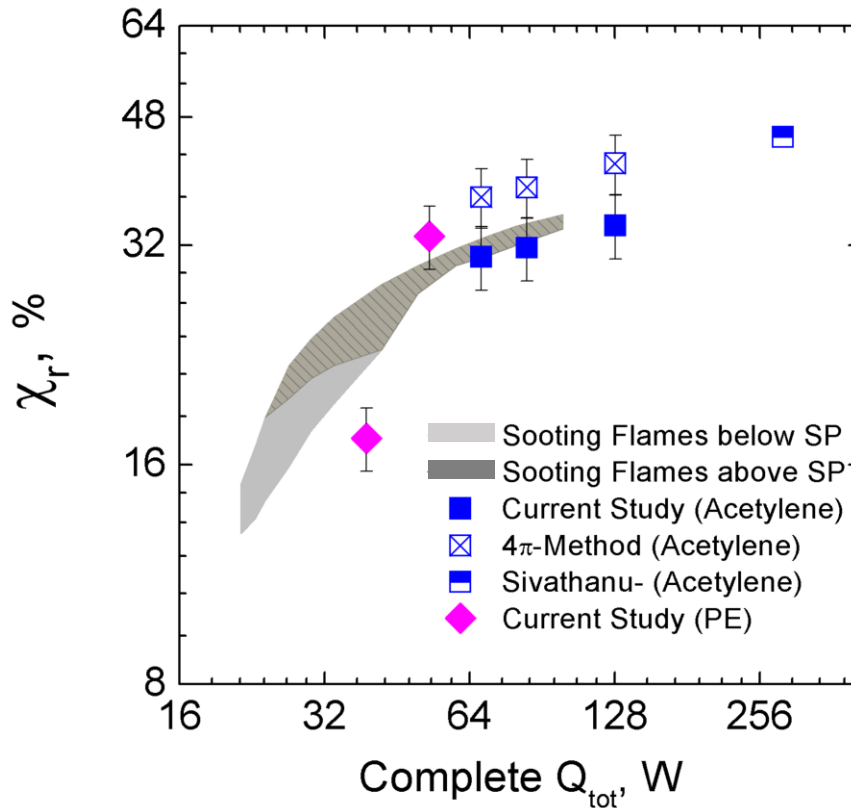


Figure 23. Measured radiative fractions for acetylene and polyethylene, in addition to literature values. The figure is plotted on a log2-log2 axis.

The polyethylene data is also presented; the lower heating rate did not reach smoke point and falls below the Markstein data that pertains to flames below the smoke point. For the higher heating rate, the flame extends beyond the smoke point and jumped considerable to the highly sooting region. Although there are no comparison values for laminar polyethylene flames, the values may be compared to those of Quintiere et al. (Quintiere, Lyon, & Crowley), who measured turbulent polyethylene flames in the cone calorimeter and calculated the radiative fraction based on the chemical heat release and the losses to the system of the cone. A value of 42% was determined for PE, which is based on a ratio of radiation lost to the chemical energy release, \dot{Q}_{chem} (Quintiere, Lyon, & Crowley). Conversely, Tewarson (Tewarson, Combustion efficiency and its radiative component, 2004) bases radiative fraction of

turbulent polymer flames on a heat of combustion found in the oxygen bomb and developed a correlation that provides a radiation fraction value of 38.9%. It can be assumed (based on the turbulent/laminar comparison done by Markstein) that the radiative fraction of turbulent flames will be higher than their laminar counterparts, which agrees with the data shown here.

3.5 Flame height versus heat release rate

A relationship often used in fire science is the relationship between flame height and heat release rate. There are many correlations of the flame height of diffusion flames as a function of heat release rate (or vice versa) depending on the geometric setup of the burner. Most of these relationships incorporate

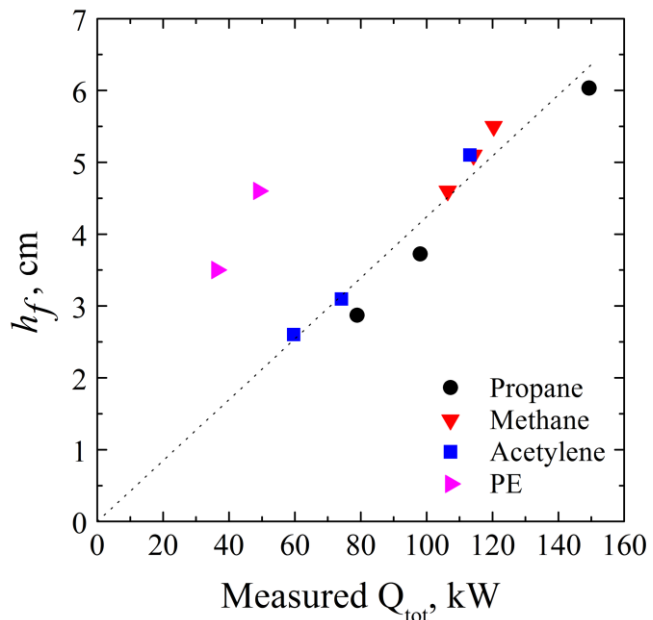


Figure 24. Flame height plotted as function of heat release rate (total HRR, using measured heat of combustion). Trendline shown for gaseous fuels.

the stoichiometric fuel to air ratio, the properties of the fuel (temperature, density, viscosity), and the volumetric flow rate. Turns (Turns, 2000) showed that there is a linear dependence of the flame length to heat release rate for circular ports, which is the geometry of the MFC setup. As can be seen in Figure 24, all of the fuels display a linear relationship with the measured heat release rate. Additionally, all of the flames of gaseous fuels converged around a single trend line that is shown in Figure 24. The

polyethylene tests varied from this trend line, likely the cause of various changes in experimental procedure, one of which is the addition of a purge gas (nitrogen) that was used to carry the volatiles to the flame region. Due to the purge gas, the flame is stretched, causing flame heights that are taller than the gaseous counterparts. Nonetheless, the results shown in Figure 24 are as expected.

Chapter 5: Conclusions and future work

5.1 Conclusions

This study presents a unique method for measuring the spatially resolved radiation intensity and the radiative fraction for laminar diffusion flames, and is the first study to measure laminar flame radiation for solid state fuels. The method presents novel measurements that resolve the spatial variations in radiation and relate these variations to the radiation heat release rate for a full picture of the radiation interactions of the environment. Due to the simplicity of the methodology as compared to previous studies, this method expedites the process of measuring the fire risk of new polymer mixtures and collecting radiation data for input to computational models.

This method shows that optical measurements of a digital camera are a valuable and simple means of determining flame properties such as flame shape and radiation intensity. With the high temporal resolution of the images, the standard error of the radius and intensity profiles are low, leading to a reduced uncertainty in the final measurements.

When compared to the values of previous studies, the radiative fractions found using this methodology varied by roughly 20% from the far-field measurements of Markstein (Markstein G. , 1984). However, when a spherically isotropic assumption of radiation was assumed to match the far-field measurements of Markstein, and the radiation heat release rate was recalculated with the position of the gauge artificially placed at 30cm, the resulting radiative fractions found agreement within error of the measurements. This highlights the fact that there may be geometric radiation effects

that are ignored when a spherically isotropic radiation assumption is, bringing into question the validity of far-field measurements for small, laminar flames.

5.2 Recommendations for future work

The method provided results that agreed with prior studies and offered a simplified method for measuring radiation properties. However, there are a number of recommendations by the author for future work that can be expanded off of this study. These recommendations are presented below.

In order to fully understand the capabilities of this method, a more robust study of polymer fuels should be conducted in order to validate the method's application to all fuel types. Although the results of polyethylene showed promising results that agreed with previous studies, polymers of different composition and flaming behaviors may present challenges to the method that may require slight alterations of the methodology. Therefore, the author recommends that various polymer fuels are tested in order to bolster the method.

Because the relation function $c(z)$ is optimized using the heat flux gauge predictions in reference to actual measurements at the gauge face, it would be of interest to increase the number of heat flux gauge locations in order to make the method more time efficient. Measuring the heat flux with an array of gauges also allows for the radiation to be measured at different periods of the flame progression and suppression for solid fuels. Although this is an expensive addition to the method, having an array of heat flux gauges measuring the flame at the same time is the ideal experimental setup.

As discussed in the beginning of this study, one motivation for studying laminar diffusion flames of polymer fuels is to better understand the scaling between laminar and turbulent flames. Markstein (Markstein G. , 1984) presented radiative fraction data of gaseous fuels, and related the radiative fractions of both laminar and turbulent flames to the smoke point (smoke point length for turbulent and heat release rate at smoke point for laminar flames). This poses a possibility for scaling between laminar and turbulent flames, which is of particular interest with polymeric fuels due to tests with small sample sizes providing radiation data for a range of flame sizes. This would pose a cost and time-efficient alternative to larger tests such as the fire propagation apparatus or the cone calorimeter. The results in Section 3.1.6 show that the peak radiation intensities for each fuel are not strongly dependent on the heat release rate of the flame, and therefore pose a possible parameter for extrapolating to turbulent flames. Additionally, by altering the definition of the flame to a radiating volume (instead of a flame sheet) and changing the accompanying mathematical description of the radiation, this method can be used with turbulent flame experiments as well. Therefore, the use of the maximum radiation intensity would be consistent between laminar and turbulent experiments.

For this study, the heating rates of the pyrolizer of the MFC were chosen based on matching the flame heights of the gaseous fuels, since the heating rate determines the rate of volatile production, and consequently the flame height. However, for the higher heating rate, the window of time where a stable flame was present was quite short, providing only a short duration to acquire images of the flame. If an optimal heating rate was found to present a sufficiently long stable flame (~7-10 seconds), in

addition to an optimized sample mass to accompany the heating rate, the uncertainty of the radius profile and heat flux gauge readings would be reduced, resulting in more precise method. Because this methodology is unique to providing a means of measuring radiative properties of solid fuels, optimizing the settings regarding the pyrolizer and sample size is recommended.

The temperature (and soot yield) are important parameters in calculations of radiation, and are the primary parameters used in computational models for resolving radiation. There is the capability of measuring temperatures of polymeric flames in the MFC apparatus, as was the work of Frances (Frances, 2014). Further validation of the methodology could be done by acquired temperature measurements using ratio pyrometry in accordance with Frances, and further use these temperatures in the radiation equation to predict the local and total flame radiation to the face of a gauge. This comparison would also pose the possibility of a correlation between the measured radiation intensity of the flame and the local temperatures of the flame.

Appendices

Appendix A: MATLAB Script- Method validation with cone formation

```
clear all
close all
clc

format long

tic
%(C) Catherine Hamel, 2016
%%User inputs
xg = 0;           %diff surface x position
yg = 35;         %diff surface y position
zg = 35;         %diff surface z position

% Cone Test

k=1;
flameheight = 30; %cone height is x units
dz = 0.1 ; %discrete element thickness- comparable to flame sheet
ugage = [0 0 -1]; %unit vector of gage face, facing directly downward
lowactive = 0;
FlameArea = 0;
steps = (flameheight/dz);

% Prepare the curvefit function for operations
syms h x y q angle
r = flameheight - x; %function defining edge of cone surface

R = subs(r,x,h); %replace "x" with symbol
"h"
Dr = diff(R,h); %differentiate the
function R
F = x^2 + y^2 - R^2; %surface function
G = gradient(F); %gradient of surface
function
r = matlabFunction(R); %convert symbolic
function to Matlab function (with handle)
f = matlabFunction(F); %convert symbolic
function to Matlab function (with handle)
gradf = matlabFunction(G); %convert symbolic
function to Matlab function (with handle)
```

Preallocations

```
Fgp_z = zeros(1,round(flameheight/dz)); dA_z = Fgp_z;
count = 0;
dAsumrow = 0;
Fgpsumrow = 0;
centerline= zeros(1,round(flameheight/dz));
```

Compute the shape factor

```
for k = 1:1
% flameheight = lowactive{k}-highactive{k};

syms h x y
R = (flameheight - (h));           %function defining radius of cross
section
dr = diff(R,h);                   %slope of radius
F = x^2 + y^2 - R^2;              %surface function
G = gradient(F);                  %gradient of the surface function (describes
the normal vector)
r = matlabFunction(R);
f = matlabFunction(F);
gradf = matlabFunction(G);
DR = -1;

N = zeros(flameheight,1);

dA1 = zeros(round(steps));
count = 0;
dAsum = 0;
dAsumrow = 0;
Fgpsum = 0;
Fgpsumrow = 0;
for z = 1:steps
    zval = lowactive+(z-1)*dz;     %z-location of loop pass
    rad = r(zval);                 %accompanying radius value at zval row
    if rad >= 0
        N = round(2*pi*rad/dz);    %number of elements in row z
        theta = NaN(1,N+1);       %pre-allocation
        dtheta = 2*pi/N;          %theta step size for row z
        s = rad*dtheta;           %arc
        length of element in height z
        Fgpsum = 0;               %reset the row's shape factor
        dAsum = 0;
        if count == 0
            radi = rad;           %for first row, pre-set
            radius
        end
        for i = 1:N               %parallel for loop to compute
            shape factor of each row
                theta(i) = dtheta*(i-1);
            %theta location of each element
```

```

        xp= rad*cos(theta(i)); %x
location at theta
        yp = rad*sin(theta(i)); %y
location at theta
        zp= zval;
%z location at theta
        xp(xp==0) = NaN;
        vgp = [(xp-xg) (yp-yg) (zp-zg)];
%vector from gage to point of interest, p
        vgp = vgp/norm(vgp);
%unit vector
        vpg = -vgp;
%vector from point of interest, p, to gage
        normal = gradf(zp,xp,yp);
        normal = normal/norm(normal);
        ux = normal(2); uy = normal(3); uz = normal(1);
        unitp = [ux uy uz];
        costheta = (dot(ugage,vgp))/(norm(ugage)*norm(vgp));
%cos of angle formed between vgp and ugage
        costhetaprime = (dot(unitp,vgp))/(norm(unitp)*norm(vgp));
%cos of angle formed between vpg and unitp
        testcostheta(z,i) = costhetaprime;
        if costhetaprime < 0
            unitp = -unitp;
            costhetaprime = 0;
        end
        Rl = sqrt((xp-xg)^2+(yp-yg)^2+(zp-zg)^2);
%magnitude of length between point and gage
        dA1 = s*sqrt(((rad-radi)).^2+(dz)^2);
%differential area of point
        Fgp = costheta*costhetaprime*dA1/pi/(Rl^2);
%shape factor of point
        dAsum = dAsum+dA1;
%summed area of row
        Fgpsum = Fgpsum +Fgp;
%summed shape factor of row
        end
        radi = rad;
        Fgp_z(z) = Fgpsum;
        dA_z(z) = dAsum;
        count = count + 1
    else
    end

    clear rad drdz theta n N s dtheta
    end
end
Fgptot = sum(Fgp_z);

```

Analytical Solution

```

s = zg-flameheight;
h = zg;
r = flameheight;
p = yg;
beta = atan(r/(h-s));
H = h/r;
P = p/r;
S = s/r;
nu = tan(beta);
angle = 0;

F12_1 = sin(beta)/pi/P*(S*sin(angle)+P*cos(angle))*(atan(H/(cos(beta)*(P^2-
S^2*nu^2)^(0.5)))-atan(S/(P^2-
S^2*nu^2)^(0.5)/cos(beta)))+1/pi*(H/P*sin(angle)+cos(angle))*atan(sqrt((P+S*nu)/(P-
S*nu)))+1/pi*(-H/P*sin(angle)*((H-S)^2*nu^2+P^2+H^2)+cos(angle)*((H-S)^2*nu^2-P^2-
H^2))*(atan(sqrt(((H-S)^2*nu+P^2+H^2+2*P*(H-S)*nu*(P+S*nu))/((H-S)^2*nu^2+P^2+H^2-
2*P*(H-S)*nu*(P-S*nu)))))/sqrt(((H-S)^2*nu^2+P^2+H^2)^2-4*P^2*(H-S)^2*nu^2));

error = abs(F12_1-Fgptot)/Fgptot
error2 = abs(F12_1-Fgptot)/F12_1

toc

```

Published with MATLAB® R2015b

Appendix B: MATLAB script- Processing code for calculation of $c(z)$

```
clear all
close all
clc

format long
%(C) Catherine Hamel, 2016
%=====
%=====
%User inputs

% Declare generic filepath, filename and extension IMPORTANT!!!
filepath='F:\Lab work 2015-2016\Radiation Fraction Propane Test August 2015\Methane
Tests\Methane_07_06\216_15_filter\Pics_1\'; %add backslash at the end if you need to
tifFiles = dir([filepath 'MF1_*.tif']); %flame picture file header
% tifFilesBackground = dir([filepath 'Background*.tif']); %background picture file
header
filename = 'ME_216_15';

HFGage = 0.570590118; %average heat flux gage reading raw
BackgroundInt = 0.08218143; %average heat flux gage background reading

VFlow = 216.0; %fuel flow, sccm
dHC = 55521; %methane 48223; %acetylene 47166; %polyethylene 50327; %propane ;
density = 0.6643908; %kg/m^3 (from AirGas)1.827; %kg/m^3 (from AirGas) %

center = 3663; %xpixel location of center of picture
burnerlength = 4480;
xlow = center-600; %lower limit x-pixels
xhigh = center+600; %upper limit x-pixels
ylow = 1; %lower limit y-pixels
yhigh = burnerlength; %upper limit y-pixels
pixeltomill = 61.94594595; %pixel to mm conversion ratio
xg = 6273;% -2.5cm      6032;% -1.5cm      6851;% -5.0cm      6506;% -3.5cm
yg = 0;
zg = 2987;% -2.5cm      3595;% -1.5cm      1426;% -5.0cm      2390; %-3.5cm

ShutterSpeed = 1/1.3; %shutter speed used while taking pictures
MaxChanVal = 65535; %65535 is max value a 16-bit channel may have

contouryes = 0; %contour = 1 if want to output contour plots of pictures;
% IF WANT CONTOUR PLOTS FOR ALL FLAMES: must make pictureGRAY a cell matrix
% that stores all picture's values

z = 0; %z=1 if want to see cutout of picture
print = 0; %print = 1 if want to export to excel
flameheightplot = 0; %plot flame height versus sccm if ==1

%=====
%=====
```



```

%read files and find mean intensity of each image
numfiles = length(tifFiles);
filenames = cell(1,numfiles);
pics = cell(1,numfiles);

count = 0;

%pre-establish the empty cell matrixes for the for loop
filenames = cell(1,numfiles);
picturemean = cell(1,numfiles);
maxpixelintensity = cell(1,numfiles);
minpixelintensity = cell(1,numfiles);
intensityIntegral = cell(1,numfiles);
intensityMean = cell(1,numfiles);
height = zeros(1,numfiles);
backgroundcount = 0;
sectionpic = cell(1,numfiles);
halfpicright = sectionpic; sectionpicdub = sectionpic;

```

Determine mean radius and intensity profiles

```

% Find Grayscale of Flame Images
sumpics = zeros((yhigh-ylow+1), (xhigh-center+1));
for k = 1:numfiles;

    filenames = strcat(filepath,tifFiles(k).name); %names of images being processed
    pics = imread(filenames); %read each of the picture files
    sectionpic = pics(ylow:yhigh, xlow:xhigh, :); %cut out section of picture
    halfpicright = pics(ylow:yhigh, center:xhigh, :); %half of picture, starting at
    center
    sectionpicdub = double(halfpicright)/ShutterSpeed;

    if z == 1
        imshow(sectionpic)
    else
    end

    for i = 1:3
        channelval(:, :, i) = sectionpicdub(:, :, i); %normalize each channels intensities
        by max 16-bit intensity
    end

    R = channelval(:, :, 1); %red channel values
    G = channelval(:, :, 2); %green channel values
    B = channelval(:, :, 3); %blue channel values

    pictureGRAY = (R+B+G)/3; %average 3 channels to get greyscale values

    pictureGRAY = pictureGRAY/MaxChanVal;
    if max(max(pictureGRAY)) >= 1
        formatSpec = 'Picture is overexposed. Use new picture set.';
        return;
    end
end

```

```

else
end

```

Find centerline and properties of grayscale image

```

minGRAY = min(min(imageGRAY));
maxGRAY = max(max(imageGRAY));

threshold = (maxGRAY-minGRAY)*0.07;    %set maximum value as 7% of maximum value

highmeanpix = imageGRAY >= threshold;    %set threshold value (double
precision value)
[rows,columns] = find(highmeanpix(:, :) == 1);    %location of the cells
that are above threshold
[blankrow, blankcolumn] = find(highmeanpix(:, :) == 0);

if isempty(rows) %if threshold value is less than maxAllGray, display error message
and stop script
    disp('The threshold is too high; No pixel reaches threshold value. Reset
threshold.')
    return;
else
end
flametip = min(rows); %maximum row where flame is detected
height(k) = burnerlength-flametip; %length of flame from burner location
highmeanpixels = imageGRAY.*double(highmeanpix); %create matrix of grayscale
picture where pixel > threshold

centerlineOG{k} = imageGRAY(:,1); %take centerline profile at first column
zcenterlineOG{k} = flip1r(1:length(centerlineOG{k})); %/height;
zcenterlineOG{k} = zcenterlineOG{k}.'; %transpose column vector

zcenterlineNORM{k} = zcenterlineOG{k}./height(k);

```

Find the edge or radius of flame

```

radius = zeros(1,length(highmeanpix));
for j = 2: length(highmeanpix)
    if isnan(double((radius(j-1)))) == 1
        radius(j) = NaN;
    else
        [rowactive, collactive] = find(highmeanpix(j, :) == 1);    %location of
the cells that are above threshold
        [blankrow, blankcoll] = find(highmeanpix(j, :) == 0);
        radius(j) = min(blankcoll);    %radius is where the first value
outside of threshold value is detected
        if max(collactive) > min(blankcoll)
            radius(j) = max(collactive)+1;    %if there are blank column before the
edge of the flame, go to the rightmost active cell and add one to get to the
equivalent blank cell
        end
    end
end

```

```

end

radius(radius == 1) = NaN;           %if the radius is stored as the first row,
convert to NaN (this applies to the rows above the flame tip)
radius(radius == 0) = NaN;

%Find z-locations of flame
nonactive = isnan(radius);           %find nonactive rows
active = find(~nonactive);           %find active row locations of picture
lowactive1 = max(active);             %lowest point on flame detected
highactive = min(active);            %highest point on flame detected

maxpixelintensity = nanmax(nanmax(imageGRAY)); %maximum pixel intensity value for
picture
minpixelintensity = nanmin(nanmin(imageGRAY)); %minimum pixel intensity value for
picture
intensityIntegral = sum(sum(highmeanpixels)); %take sum of all values > threshold
intensityMean = mean(mean(highmeanpixels(highmeanpixels~=0))); %take mean of all
values > threshold

activepixels = length(rows); %number of pixels above the threshold
pixelnormIntegral = intensityIntegral./activepixels(1,1); %the picture intensity
normalized by number of active pixels

```

Fit curve to the radius values

```

values = burnerlength - active;       %z-locations of radius locations
radiusgood = radius(~isnan(radius)); %all detected radius locations
for i = 1:length(radiusgood)-1        %for loop to cutoff the active
cells
    m = i+1;
    if (abs(radiusgood(m)-radiusgood(m-1))) >= 25 %if two adjacent rows differ in
radius by more than 10 pixels, discard
        radiusgood(m) = NaN;
    end
    if isnan(radiusgood(m-1));          %if the row above is NaN, then
the current row is NaN
        radiusgood(m) = NaN;
    end
end
radiusgood1{k} = radiusgood(~isnan(radiusgood)); %find all radius values
radiusgood1{k} = flipud(radiusgood1{k}.');
values1{k} = values(1:length(radiusgood1{k})); %find all
accompanying z-values for radius locations
values1{k} = flipud(values1{k}.');
ztest = 1:length(radius); %values 1 through length of
radius locations
znew = burnerlength-ztest; %flip the coordinates to have
0 corresponding to top of burner
piclength(k) = length(radiusgood1{k});
end

```

Left Hand Side

```
for n = 1:numfiles;

    k = numfiles + n;
    filenames = strcat(filepath,tifFiles(n).name); %names of images being processed
    pics = imread(filenames); %read each of the picture files
    sectionpic = pics(ylow:yhigh, xlow:xhigh, :); %cut out section of picture
    halfpicleft = pics(ylow:yhigh, xlow:center, :); %half of picture, starting at
    center
    sectionpicdub = double(halfpicleft)/ShutterSpeed;

    if z == 1
        imshow(sectionpic)
    else
    end

    for i = 1:3
        channelval(:, :, i) = sectionpicdub(:, :, i); %normalize each channels intensities
        by max 16-bit intensity
    end

    R = channelval(:, :, 1); %red channel values
    G = channelval(:, :, 2); %green channel values
    B = channelval(:, :, 3); %blue channel values

    pictureGRAY = (R+B+G)/3; %average 3 channels to get greyscale values
    pictureGRAY = flip1r(pictureGRAY);

    pictureGRAY = pictureGRAY/MaxChanVal;
    if max(max(pictureGRAY)) >= 1
        formatSpec = 'Picture is overexposed. Use new picture set.';
        return;
    else
    end
end
```

Find centerline and properties of grayscale image

```
minGRAY = min(min(pictureGRAY));
maxGRAY = max(max(pictureGRAY));

threshold = (maxGRAY-minGRAY)*0.07; %set maximum value as 7% of maximum value

highmeanpix = pictureGRAY >= threshold; %set threshold value (double
precision value)
[rows, collumns] = find(highmeanpix(:, :) == 1); %location of the cells
that are above threshold
[blankrow, blankcollumn] = find(highmeanpix(:, :) == 0);

if isempty(rows) %if threshold value is less than maxAllGray, display error message
and stop script
    disp('The threshold is too high; No pixel reaches threshold value. Reset
```

```

threshold.')]
    return;
else
end
flametip = min(rows); %maximum row where flame is detected
height(k) = burnerlength-flametip; %length of flame from burner location
highmeanpixels = pictureGRAY.*double(highmeanpix); %create matrix of grayscale
picture where pixel > threshold

centerlineOG{k} = pictureGRAY(:,1);
zcenterlineOG{k} = flip1r(1:length(centerlineOG{k}));%/height;
zcenterlineOG{k} = zcenterlineOG{k}.';

zcenterlineNORM{k} = zcenterlineOG{k}./height(k);

```

Find the edge or radius of flame

```

radius = zeros(1,length(highmeanpix));
for j = 2: length(highmeanpix)
    if isnan(double((radius(j-1)))) == 1
        radius(j) = NaN;
    else
        [rowactive, collactive] = find(highmeanpix(j,:) == 1); %location of
the cells that are above threshold
        [blankrow, blankcoll] = find(highmeanpix(j,:) == 0);
        radius(j) = min(blankcoll); %radius is where the first value
outside of threshold value is detected
        if max(collactive) > min(blankcoll)
            radius(j) = max(collactive)+1; %if there are blank column before the
edge of the flame, go to the rightmost active cell and add one to get to the
equivalent blank cell
        end
    end
end

radius(radius == 1) = NaN; %if the radius is stored as the first row,
convert to NaN (this applies to the rows above the flame tip)
radius(radius == 0) = NaN;

%Find z-locations of flame
nonactive = isnan(radius); %find nonactive rows
active = find(~nonactive); %find active row locations of picture
lowactive1 = max(active); %lowest point on flame detected
highactive = min(active); %highest point on flame detected

maxpixelintensity = nanmax(nanmax(pictureGRAY)); %maximum pixel intensity value for
picture
minpixelintensity = nanmin(nanmin(pictureGRAY)); %minimum pixel intensity value for
picture
intensityIntegral = sum(sum(highmeanpixels)); %take sum of all values > threshold
intensityMean = mean(mean(highmeanpixels(highmeanpixels~=0))); %take mean of all

```

```
values > threshold
```

```
activepixels = length(rows); %number of pixels above the threshold  
pixelnormIntegral = intensityIntegral./activepixels(1,1); %the picture intensity  
normalized by number of active pixels
```

Fit curve to the radius values

```
values = burnerlength - active;           %z-locations of radius locations  
radiusgood = radius(~isnan(radius));     %all detected radius locations  
for i = 1:length(radiusgood)-1           %for loop to cutoff the active  
    cells  
        m = i+1;  
        if (abs(radiusgood(m)-radiusgood(m-1))) >= 25 %if two adjacent rows differ in  
            radius by more than 10 pixels, discard  
            radiusgood(m) = NaN;  
        end  
        if isnan(radiusgood(m-1));           %if the row above is NaN, then  
            the current row is NaN  
            radiusgood(m) = NaN;  
        end  
    end  
radiusgood1{k} = radiusgood(~isnan(radiusgood)); %find all radius values  
radiusgood1{k} = flipud(radiusgood1{k}.');  
values1{k} = values(1:length(radiusgood1{k})); %find all  
    accompanying z-values for radius locations  
values1{k} = flipud(values1{k}.');  
ztest = 1:length(radius); %values 1 through length of  
    radius locations  
znew = burnerlength-ztest; %flip the coordinates to have  
    0 corresponding to top of burner  
piclength(k) = length(radiusgood1{k});  
end  
  
centervals = [centerlineOG{1,:}];  
zcenterline = [zcenterlineOG{1,:}];  
  
clear centerlineOG zcenterlineOG  
  
% Average centerline profiles to get mean profile  
for m = 1:length(centervals)  
    centerlineOG(m) = nanmean(centervals(m,:)); %mean radius value  
    zcenterlineOG(m) = nanmean(zcenterline(m,:)); %mean z-val  
    stdCENTER(m) = nanstd(centervals(m,:)); %std at each height  
    errorCENTER(m) = stdCENTER(m)/sqrt(length(radiusgood1)); %standard error at each  
    height  
end  
  
%average radius profiles to get mean profile  
for i = 1:length(radiusgood1)  
    for j = 1:max(piclength)
```

```

        if j > piclength(i)
            values2(j,i) = NaN;
            radiusgood2(j,i) = NaN;
        else
            values2(j,i) = values1{i}(j);
            radiusgood2(j,i) = radiusgood1{i}(j);
        end
    end
end

for l = 1:length(radiusgood2)
    meanROW(l) = nanmean(radiusgood2(l,:)); %mean radius value
    meanVAL(l) = nanmean(values2(l,:)); %mean z-val
    stdROW(l) = nanstd(radiusgood2(l,:)); %std at each height
    errorROW(l) = stdROW(l)/sqrt(length(radiusgood1)); %standard error at each
    height
end

% Fit the profiles
curvefitflip = fit(meanVAL.',meanROW.','poly6'); %curvefit for radius profile
cent = fit(zcenterlineOG.',centerlineOG.','gauss1'); %curvefit for intensity profile

figure
h = errorbar(meanVAL,meanROW,errorROW. ');
set(h,'color','w');
hold on; plot(curvefitflip,meanVAL.',meanROW. ')

figure
e = errorbar(zcenterlineOG.',centerlineOG.',errorCENTER. ');
set(e,'color','w')
hold on; plot(cent, zcenterlineOG.', centerlineOG. ')

```

Calculate the Shape Factor from Flame the Gauge

```

dz = 1; %discrete element thickness- comparable to flame sheet
ugage = [-1 0 0]; %unit vector of gage face, facing center of burner

flameheight = round(max(meanVAL));
lowactive = round(min(meanVAL));

xg = xg-center; %/pixel to mill; %convert pixel lengths
to physical length (mm)
yg = yg; %/pixel to mill; %convert pixel lengths to
physical length (mm)
zg = burnerlength - zg; %/pixel to mill; %convert
pixel lengths to physical length (mm)

% Prepare the curvefit function for operations
syms h x y q angle
r = sym( formula( curvefitflip ) ); %convert curvefit to
symbolic function
cn = coeffnames( curvefitflip ); %stored curvefit

```

```

coefficient variables
cv = coeffvalues( curvefitflip );           %stored curvefit
coefficient values
r = subs( r, cn, cv.' );                   %symbolic function with
coefficients

ic = sym(formula(cent));
icn = coeffnames(cent);
icv = coeffvalues(cent);
ic = subs(ic,icn,icv.' );
ic = subs(ic,x,h);
Ic = matlabFunction(ic);

R = subs(r,x,h);                           %replace "x" with symbol
"h"
Dr = diff(R,h);                             %differentiate the
function R
F = x^2 + y^2 - R^2;                         %surface function
G = gradient(F);                            %gradient of surface
function
r = matlabFunction(R);                      %convert symbolic
function to Matlab function (with handle)
f = matlabFunction(F);                     %convert symbolic
function to Matlab function (with handle)
gradf = matlabFunction(G);                 %convert symbolic
function to Matlab function (with handle)

%Pre-allocations
Fgp_z = zeros(1,round(flameheight/dz)); dA_z = Fgp_z;
count = 0;
dAsumrow = 0;
Fgpsumrow = 0;
centerline= zeros(1,flameheight/dz);

% Compute the shape factor
for z = 1:(flameheight)/dz;
    zval = lowactive+(z-1)*dz;              %z-location of loop pass
    rad = double(subs(r,h,zval));           %accompanying radius value at
zval row
    centerline(z) = double(subs(Ic,h,zval));
    if rad >= 0
        % drdz = double(subs(dr,h,z));
        N = round(2*pi*rad/dz);             %number of elements in row z
        theta = NaN(1,N+1);                 %pre-allocation
        dtheta = 2*pi/N;                   %theta step size for row z
        s = rad*dtheta;                     %arc
length of element in height z
        % n = N+1;                          %number of step sizes
        Fgpsum = 0;                          %reset the row's shape factor
        dAsum = 0;
        if count == 0
            radi = rad;                     %for first row, pre-set
radius

```



```

end
    for i = 1:N %parallel for loop to compute
shape factor of each row
        theta(i) = dtheta*(i-1);
%theta location of each element
        xp= rad*cos(theta(i)); %x
location at theta
        yp = rad*sin(theta(i)); %y
location at theta
        zp= zval;
%z location at theta
        xp(xp==0) = NaN;
        vgp = [(xp-xg) (yp-yg) (zp-zg)];
%vector from gage to point of interest, p
        vgp = vgp/norm(vgp);
%unit vector
        vpg = -vgp;
%vector from point of interest, p, to gage
        normal = gradf(zp,xp,yp);
        normal = normal/norm(normal);
        ux = normal(2); uy = normal(3); uz = normal(1);
        unitp = [ux uy uz];
        costheta = (dot(ugage,vgp))/(norm(ugage)*norm(vgp));
%cos of angle formed between vgp and ugage
        costhetaprime = (dot(unitp,vgp))/(norm(unitp)*norm(vgp));
%cos of angle formed between vgp and unitp
        if costhetaprime < 0
            unitp = -unitp;
            costhetaprime = (dot(unitp,vgp))/(norm(unitp)*norm(vgp));
%cos of angle formed between vgp and unitp
        end
        Rl = sqrt((xp-xg)^2+(yp-yg)^2+(zp-zg)^2);
%magnitude of length between point and gage
        dA1 = s*sqrt((rad-radi).^2+(dz)^2);
%differential area of point
        Fgp = costheta*costhetaprime*dA1/(Rl^2);
%shape factor of point
        dAsum = dAsum+dA1;
%summed area of row
        Fgpsum = Fgpsum +Fgp;
%summed shape factor of row
    end
    radi = rad;
    Fgp_z(z) = Fgpsum;
    dA_z(z) = dAsum;
    count = count + 1
else
end

clear rad drdz theta n N s dtheta
end
Fgptot = sum(Fgp_z); %total shape factor flame to gage
dAflame = sum(dA_z); %total area of flame

```

```
height = mean(height(:));  
IntVF = Fgp_z.*centerline; %kw/m^2  
IntVFtot = sum(IntVF(:));  
const = (HFgage-BackgroundInt)/IntVFtot;
```

Save Outputs

```
save(filename,'lowactive','highactive','curvefitflip','pixeltomill','centerline','radiusgood','values','cent','zcenterlineOG','errorROW','errorCENTER','height','centerlineOG','Fgp_z','const','dA_z','meanVAL','meanROW')
```

[Published with MATLAB® R2015b](#)

Appendix B: MATLAB script-Processing code for calculation of χ_r

```
clear all
close all
clc

%(C) Catherine Hamel, 2016

format long
```

Inputs

```
filename = 'PR_106_25_4percent.mat';
filenamew = 'PR_106_4percent_FINAL.mat';

% Constants for relation function:
a = -0.006;
b = 17.651;
c = 19.75;

% Fuel conditions:
VFlow = 106.0;
dHc = 46498; %propane 35494; %acetylene 51271; %methane 51083; %
density = 1.8316; %g/m^3- propane 1.0720; %g/m^3- acetylene 0.6569; %g/m^3-
methane
dz = 1;

fittype = 'poly'; %use 'poly' if polynomial fit for relation function; use 'linear'
for linear fit

load(filename)
flameheight = round(max(meanVAL));

if strcmp('poly',fittype) == 1;
    for z = 1:flameheight/dz;
        zval(z) = (lowactive+(z-1)*dz)/pixeltomill; %z-location of loop pass
        constant(z) = a*zval(z).^2 + b*zval(z) + c;
    end
elseif strcmp('linear',fittype) ==1;
    for z = 1:length(dA_z)/dz;
        zval(z) = (lowactive+(z-1)*dz)/pixeltomill; %z-location of loop pass
        constant(z) = a*zval(z) + b;
    end
end

Qrad = 2*pi*sum(constant.*centerline.*dA_z)/(pixeltomill*1000)^2;
mdot = VFlow*(1/60/100^3)*density*0.9926; %kg/s
Qtot = mdot*dHc; %kw
Xr = 1.03*Qrad/Qtot;

save(filenamew, 'dHc', 'lowactive', 'highactive', 'curvefitflip', 'pixeltomill', 'centerl
```

```
ine','radiusgood','values','cent','zcenterlineOG','errorROW','errorCENTER','height','centerlineOG','Fgp_z','Xr','const','dA_z','meanVAL','meanROW','Qrad','Qtot')
```

Published with MATLAB® R2015b

Bibliography

- Brookes, S., & Moss, J. (1999). Predictions of soot and thermal radiation properties in confined turbulent jet diffusion flames. *Combustion and Flame*, 116(4), 486-503.
- Chung, B., & Sumitra, P. (1972). Radiation shape factors from plane point sources. *Journal of Heat Transfer*, 94(3), 328-330.
- Chung, B., Kermani, M., & Naraghi, M. (1984). A formulation of radiation view factors from conical surfaces. *American Institute of Aeronautics and Astronautics Journal*, 22(3), 429-436.
- de Ris, J., & Cheng, X. (1976). The Role of Smoke-Point in Material Flammability Testing. *Fire Safety Science*, 31(3), 301-312.
- Demarco, R., Nmira, F., & Consalvi, J. (2013). Influence of thermal radiation on soot production in Laminar axisymmetric diffusion flames. *Journal of Quantitative Spectroscopy and Radiative Transfer*, 120, 52-69.
- Ding, X. (2013). *Design and implementation of the flaming combustion calorimeter: Master's thesis*. College Park: University of Maryland.
- Escudero, F., & al., e. (2016). Unified behavior of soot production and radiative heat transfer in ethylene , propane and butane axisymmetric laminar diffusion flames at different oxygen indices. *Fuel*, 183, 668-679.
- Frances, C. (2014). *A Non-Intrusive Method for Temperature Measurements in Flames Produced by Milligram-Sized Solid Samples: Master's Thesis*. College Park: University of Maryland.
- Gore, J., & Faeth, G. (1986). Structure and Spectral Radiation Properties of Turbulent Ethylene/air Diffusion Flames. *Twenty-first Symposium (International) on Combustion*, 1521-1531.
- Gore, J., & Zhan, N. (1996). NO(x) emission and major species concentrations in partially premixed laminar methane/air co-flow jet flames. *Combustion and Flame*, 105(3), 414-427.
- Goulay, F. S. (2010). Effect of the wavelength dependence of the emissivity on inferred soot temperatures measured by spectrally resolved laser-induced incandescence. *Applied Physics B: Lasers and Optics*, 100(3), 655-663.
- Hankinson, G., & Lowesmith, B. (2012). A consideration of methods of determining the radiative characteristics of jet fires. *Combustion and Flame*, 159(3), 1165-1177.
- Hurley, M. J., Gottuk, D., Hall, J. R., Harad, K., Kuligowski, E., Puchovsky, M., . . . Wiecek, C. (2016). *SFPE Handbook of Fire Protection Engineering, Fifth Ed*. New York: Springer.
- Jeng, S., & Faeth, G. (1984). Radiative Heat Fluxes Near Turbulent Buoyant Methane Diffusion Flames. *Heat Transfer*, 106(4), 886-888.

- Klote, J. H. (2012). Equations for Steady Atrium Smoke Exhaust. In J. H. Klote, J. A. Milke, P. G. Turnbull, A. Kashef, & M. J. Ferreira, *Handbook of Smoke Control Engineering* (pp. 333-351). Atlanta: ASHRAE.
- Kreyszig, E. (1999). Gradient of a Scalar Field Directional Derivative. In E. Kreyszig, *Advanced Engineering Mathematics* (8 ed., p. 449). New York: John Wiley & Sons, Inc.
- Lyon, R., Walters, R., Stoliarov, S., & Safronava, N. (2013). *Principles and practice of microscale combustion calorimetry DOT/FAA/TC-12/53*. Atlantic City: Federal Aviation Administration William J. Hughes Technical Center .
- Markstein, G. (1981). Scanning-radiometer measurements of the radiance distribution in PMMA pool fires. *Symposium (International) on Combustion*, 18(1), 537-547.
- Markstein, G. (1984). Relationship between smoke point and radiant emission from buoyant turbulent and laminar diffusion flames. *Proceedings of the Twentieth Symposium (International) on Combustion*, 1055-1061.
- Markstein, G., & De Ris, J. (1985). Radiant emission and absorption by laminar ethylene and propylene diffusion flames. *Symposium (International) on Combustion*, 20(1), 1637-1646.
- McGrattan, K., McDermott, R., Hostikka, S., & Floyd, J. (2010). *Fire dynamics simulator (version 5) user's guide NIST special publication 1019-5*. Gaithersburg, Maryland, USA: NIST Building and Fire Research Laboratory.
- Modak, A. (1981). The burning of large pool fires. *Fire Safety Journal*, 3(3), 177-184.
- Orloff, L. (1981). Simplified radiation modeling of pool fires. *Symposium (International) on Combustion*, 18(1), 549-561.
- Quintiere, J., Lyon, R., & Crowley, S. (2016). An exercise in obtaining flame radiation fraction from the cone calorimeter. *Fire and Materials*, 40, 861-872.
- Raffan-Montoya, F., Ding, X., & Stoliarov, S. (2015). Measurement of heat release in laminar diffusion flames fueled by controlled pyrolysis of milligram-sized solid samples: Impact of bromine- and phosphorus-based flame retardants. *Combustion and Flame*, 16(12), 4660-4670.
- Rankin, B., Blunck, D., & Katta, V. (2012). Experimental and computational infrared imaging of bluff body stabilized laminar diffusion flames. *Combustion and Flame*, 159(9), 2841-2843.
- Sivathanu, Y., & Gore, J. (1993). Total Radiative Heat Loss in Jet Flames from Single Point Radiation Flux Measurements. *Combustion and Flame*, 94, 265-270.
- Sivathanu, Y., & Gore, J. (1994). Coupled radiation and soot kinetics calculations in laminar acetylene/air diffusion flames. *Combustion and Flame*, 97(2), 161-172.
- Tewarson, A. (2004). Combustion efficiency and its radiative component. *Fire Safety Journal*, 39(2), 131-141.
- Tewarson, A. (2008). Generation of Heat and Gaseous, Liquid, and Solid Products in Fires. In P. Dinunno, & Dougal, *SFPE Handbook of Fire Protection Engineering, 4th Ed.* (pp. 3-109 - 3-194). Boston: National Fire Protection Engineering Association.

- Turns, S. (2000). *An Introduction to Combustion: Concepts and Applications*. Boston: WCB/McGraw-Hill.
- White, J., Link, E., & Trouve, A. (2015). Radiative Emissions Measurements from a Buoyant , Turbulent Line Flame under Oxidizer-Dilution Quenching Conditions. *Fire Safety Journal*, 76, 74-84.
- Zheng, Y., Barlow, R., & Gore, J. (2003). Measurements and Calculations of Spectral Radiation Intensities for Turbulent Non-Premixed and Partially Premixed Flames. *Journal of Heat Transfer*, 125(4), 678-686.

